



Selective electrooxidation of methane to formic acid by atomically dispersed CuO_x and its induced Lewis acid sites on V_2O_5 in a tubular electrode

Hao Tian, Zi-Yang Zhang, Hui Fang, Han Jiao, Tong-Tong Gao, Jie-Tian Yang, Lei Bian, Zhong-Li Wang^{*}

Tianjin Key Laboratory of Applied Catalysis Science & Technology, School of Chemical Engineering and Technology, Tianjin University, Tianjin 300072, China

ARTICLE INFO

Keywords:

Electrocatalysis
Methane conversion
Atomically dispersed $\text{CuO}_x/\text{V}_2\text{O}_5$
Lewis acid sites
Tubular electrode

ABSTRACT

Electrocatalytic oxidation of methane (CH_4) to value-added chemicals is an attractive approach to directly use natural gas. Herein, we synthesize $\text{CuO}_x/\text{V}_2\text{O}_5$ composite catalysts in the hollow porous titanium tubes for selective electrooxidation of CH_4 to formic acid (FA). The complexed Cu^{2+} ions achieve atomic-level dispersion on the V_2O_5 surface, and then transform into atomically dispersed CuO_x during heat treatment, forming Cu-O-V bonds. Interestingly, atomically dispersed CuO_x simultaneously induces the generation of abundant oxygen vacancies with strong Lewis acid activity. Moreover, the porous tubular electrode realizes the directional transmission of CH_4 gas and create rich gas-liquid-solid three-phase reaction interfaces. The optimized active components and electrode structure achieve the Faradaic efficiency of FA up to 92 % at the current density of 14.4 mA cm^{-2} . Mechanism research indicates that atomically dispersed CuO_x and its induced Lewis acid sites promote the electrooxidation of H_2O and the adsorption-activation of CH_4 to produce $^*\text{OH}$ and $^*\text{CH}_3$.

1. Introduction

Methane (CH_4) is the main hydrocarbon component of plentiful natural gas, biogas, shale gas, and gas hydrates (combustible ice), and due to its vast reserves on the earth, it is considered as a promising feedstock for various chemical products [1,2]. Converting CH_4 to liquid fuels or chemicals by CH_4 oxidation reaction also avoids the greenhouse effect caused by the leakage of gaseous CH_4 , which is 30 times greater than CO_2 . However, as CH_4 has a stable regular tetrahedral structure and high C-H chemical bond energy (439 kJ mol^{-1}), which makes CH_4 conversion at ambient conditions extremely challenging and even considered as the holy grail of catalysis [3]. The typical thermos-catalytic processes such as steam reforming followed by gas-phase conversion often require high temperatures and pressures and suffer from catalyst poisoning during long-term operation due to coking. Therefore, it is necessary to develop new strategies for direct CH_4 conversion under mild conditions.

Electrochemical redox reactions have been employed to breakdown various stable chemicals, such as water (H_2O) and carbon dioxide (CO_2) [4,5]. Recently, electrocatalytic CH_4 oxidation reaction (eMOR) has

emerged as a remarkable technology that benefits from the desirable coupling of renewable electricity and CH_4 utilization [6–8]. This provides an approach to generate active oxygen species (e.g., $^*\text{OH}$ and O^{2-}) by selecting the proper electrocatalysts and working potentials [9–11]. In addition, solvation by the liquid medium stabilizes reaction intermediates and immediately extracts the product. Up to now, several types of electrocatalytic systems have been proven to convert CH_4 to various liquid phase products at room temperature. For example, NiO/ZrO_2 [12], $\text{Co}_3\text{O}_4/\text{ZrO}_2$ [13], $\text{NiCo}_2\text{O}_4/\text{ZrO}_2$ [14], CuO/ZrO_2 [15], CuO/CeO_2 [16], NiO/ZnO [17], and $\text{Rh}/\text{Al}_2\text{O}_3$ [18] composite catalysts combined with the electrolyte of Na_2CO_3 or KHCO_3 aqueous solution can oxidize CH_4 to CH_3OH , $\text{CH}_3\text{CH}_2\text{CH}_2\text{OH}$, $\text{CH}_3\text{CH}_2\text{COOH}$, etc. through electrocatalytic reactions, where the maximum current density can reach 13.4 mA cm^{-2} for the production of $\text{CH}_3\text{CH}_2\text{CH}_2\text{OH}$. In another type of system, cobalt-nickel (Co-Ni) spinel [19] and Cu-Ti bimetallic oxide [20] catalysts in a Cl^- -mediated environment oxidized CH_4 to CH_3Cl and mixtures of CH_3OH and HCOOH , respectively, with partial oxidation current densities of 19.5 mA cm^{-2} (FE < 10 %) and 11.2 mA cm^{-2} (FE ~ 28 %) at ambient conditions, respectively. When the reaction temperature increases to 40°C , the FE of the mixtures of

^{*} Corresponding author.

E-mail address: wang.zhongli@tju.edu.cn (Z.-L. Wang).

<https://doi.org/10.1016/j.apcatb.2024.124001>

Received 18 July 2023; Received in revised form 17 March 2024; Accepted 21 March 2024

Available online 22 March 2024

0926-3373/© 2024 Elsevier B.V. All rights reserved.

CH₃OH and HCOOH increases to ~72 % and the current density increases to ~26 mA cm⁻². In addition, NiO/Ni interface [21], iron-nickel hydroxide (Fe-Ni-OH) nanosheets [22], and Fe-N-C single atom catalysts [23] in alkaline electrolytes can also oxidize CH₄ to ethanol with the maximum current density of only ~7.0 mA cm⁻² and FE of 85 %. Although some progress has been made in electrocatalytic oxidation of CH₄, the oxidation current density and the FE of the products are still relatively low, which is far from industrial application.

The critical steps of eMOR in aqueous electrolytes are the activation of CH₄ molecules and formation of adsorbed oxidant species such as active oxygen (•OH) [24,25]. The theoretical calculation results show that there is the linear relationship between CH₄ activation energy and active oxygen binding energy for a single active site, which makes it difficult to improve both activity and selectivity simultaneously [26]. Double active site synergy can effectively overcome the shortcomings of a single site, so improving activity and selectivity requires the construction of a catalytic system with two component interactions to promote the activation and oxidation. Moreover, another challenge for CH₄ oxidation activity in aqueous media is the low solubility of CH₄ (1.30 mM in water at STP) [27], which greatly limits the diffusion of CH₄ to the electrode surface, resulting in a lower current density. Therefore, to enhance the current density of eMOR, it is necessary to design a reasonable electrode to enhance the mass transfer of CH₄. On the other hand, formic acid (FA) is an important chemical raw material that is widely used in industries such as pharmaceuticals, fuel cells, leather, printing and dyeing, textiles, rubber, and pesticides. The industrial manufacturing of FA involves an energy and cost-intensive process based on a high-temperature/high-pressure synthesis using a mixture of CO and methanol followed by the subsequent hydrolysis of the resulting methyl formate. Due to the energy consumed in this process, the price of FA is four times that of methanol, so finding alternative ways to produce FA would be economically beneficial.

In this work, we synthesize atomically dispersed CuO_x/V₂O₅ composite catalysts on hollow porous titanium (Ti) tubes for selective electrooxidation of CH₄ to FA. Honeycomb-like V₂O₅ formed by winding ultra-long nanoribbons is grown in situ on Ti tube substrates using hydrothermal methods. Then, atomic-level dispersion of Cu²⁺ ions supported on V₂O₅ is achieved under the dispersion and complexation of polyvinylpyrrolidone (PVP) and citric acid (C₆H₈O₇). During the heat treatment process, Cu ions react with O ions to produce atomically dispersed CuO_x active sites, which are bonded on the surface of V₂O₅ through Cu-O-V bonds. Due to the fact that the generated Cu species are not specific stoichiometric compounds, CuO_x is used to represent the product (x represents the number of bonded O). Interestingly, atomically dispersed CuO_x simultaneously induces the generation of abundant oxygen vacancies (O_v) with strong Lewis acid activity. Moreover, the porous tubular electrode realizes the directional transmission of CH₄ gas in the pores and create rich solid-liquid-gas three-phase reaction interfaces. Based on the advantages of active components and electrode structure, the optimized catalyst achieves the Faradaic efficiency of FA up to 92 % at the current density of 14.4 mA cm⁻² in the Na₂SO₄ electrolyte at ambient conditions. The electron paramagnetic resonance (EPR), in-situ Raman, and attenuated total reflectance Fourier transform infrared (ATR-IRAS) spectra show that atomically dispersed CuO_x and its induced Lewis acid sites on V₂O₅ promote the electrooxidation of H₂O and the adsorption-activation of CH₄ to produce two key intermediates •OH and •CH₃, both of which react to produce FA through a series of intermediates such as •CH₃, •OCH₃, HCHO• and •COOH. Density function theory calculations exhibit an obviously electron transfer behavior from atomically dispersed CuO_x to V₂O₅, which not only improves the conductivity of CuO_x/V₂O₅, but also reduces the reaction free energies of H₂O dissociation and CH₄ activation. Furthermore, the coupling of CH₄ electrooxidation and CO₂ electroreduction is verified and realizes the simultaneous generation of FA at the anode and cathode. This work will promote the development of efficient electrochemical systems with atomic-level dispersion catalysts for the

utilization of CH₄.

2. Experimental

2.1. Synthesis of catalysts

The V₂O₅ nanoribbons was prepared by the hydrothermal method reported elsewhere [28]. 0.35 g NH₄VO₃ and 0.42 g H₂C₂O₄ were dissolved in a mixture solution of 50 mL deionized water and stirred for 30 min. The porous Ti tube was sonicated in the above solution for 30 min and transferred to a Teflon autoclave, which was then transferred to an autoclave and held at 180 °C for 24 h. When the Teflon autoclave was naturally cooled to room temperature, and V₂O₅ supported on Ti tube was taken out and washed several times by anhydrous ethanol and deionized water, and then was dried for 12 h in a vacuum oven at 80 °C. In order to improve the crystallinity of the V₂O₅ catalyst, the sample was calcined in a muffle furnace under air atmosphere at 300 °C for 2 h. For the loading of Cu ions, 7 mM Cu(NO₃)₂, 0.48 g PVP and 0.76 g H₂C₂O₄ were dispersed in 40 mL of H₂O. Then, V₂O₅ supported on Ti tube was dispersed in this mixture solution for 30 min. The V₂O₅ loaded with Cu precursors was dried at room temperature for 24 h. Then the Cu²⁺/V₂O₅ precursors were calcined at 500 °C for 2 h in a muffle furnace under air atmosphere to produce atomically dispersed CuO_x/V₂O₅ composite catalysts. For comparison, single component V₂O₅ or CuO supported on Ti tube were synthesized under similar conditions.

2.2. Characterizations

Scanning electron microscopy (SEM) images were obtained on an Apreo S field emission scanning electron microscopy. Transmission electron microscopy (TEM) images were conducted on a JEOL F200 transmission electron microscope with an acceleration voltage 200 kV. The high-resolution scanning transmission electron microscopy high-angle annular dark-field (STEM-HAADF) images were collected on a Thermo Fisher Scientific Themis Z TEM/STEM with probe and image correctors. X-ray diffraction was conducted on a Bruker D8 Focus X-ray diffractometer using Cu Kα radiation (λ = 0.15418 nm) with the tube voltage and current of 40 kV and 40 mA, respectively. Raman spectra (Horiba) were recorded on a confocal Raman microscope equipped with an Ar laser. Electron paramagnetic resonance (EPR) was carried out on JES-FA200. And, the 5,5-Dimethyl-1-pyrroline-N-oxide (DMPO) was employed to trap the •OH and •CH₃ by the EPR, and the reaction under the conditions as follows: center field of 3290 G, sweep width of 100 G, microwave with a frequency of 9.89 GHz and power of 2.0 mW at 25 °C. X-ray photoelectron spectroscopy (XPS) was conducted on the Thermo K-Alpha⁺ instrument. X-ray radiation source was Al Kα (hν = 1486.6 eV) with X-ray power of 150 W and spot size was 400 μm. The X-ray absorption fine structure (XAFS) measurements were performed to probe the valence state and the coordination of Cu and V species (XAFS-500-A, Anhui Speccreation Instruments Co., Ltd, China). The obtained spectra were processed using ATHENA and extended x-ray absorption fine structure (EXAFS) spectra were fitted using ARTEMIS in Demeter software package. The adsorption isotherms of CH₄ were determined at 25 °C in the pressure range of 0–1 atm on a Belsorp max device.

2.3. Electrochemical CH₄ oxidation and product analysis

The electrocatalytic oxidation test was carried out on a three-electrode system in an H-type cell on a CHI 760E electrochemical workstation by using catalysts supported porous Ti tube as the working electrode, Pt as the counter electrode, and a saturated calomel electrode (SCE) as the reference electrode. An aqueous solution containing 0.1 M Na₂SO₄ was used as the electrolyte and Nafion 211 membrane was used to separate the cathode and anode chambers. The polarization curves were converted from linear sweep voltammetry (LSV, 90 % iR-

compensation), and the scan rate was 10.0 mV s^{-1} . All the tests were carried out at 25°C . CH_4 gas flowed through the Ti tube wall and the flow rate was 7.5 sccm during electrolysis. For the coupling of CO_2 electroreduction, the cathode used Bi_2O_3 supported on carbon tubes instead of Pt electrodes and the flow rate of CO_2 was 20.0 sccm . The CH_4 oxidation or CO_2 reduction products were recorded by high-performance liquid chromatography (HPLC) (Shimadzu, LC-20A) equipped with an Aminex HPX-87 H ion exclusion column ($300 \text{ mm} \times 7.8 \text{ mm}$). The column temperature was 35°C and the detector

temperature was 35°C ; the mobile phase was $5 \text{ mM H}_2\text{SO}_4$ at a flow rate of 0.6 mL min^{-1} . The liquid products also were analyzed and quantified by Varian 600 MHz proton NMR (^1H NMR) with pre-saturation water suppression optimization. Specifically, $150 \mu\text{L D}_2\text{O}$ and $500 \mu\text{L}$ liquid aliquots collected from an electrocatalytic reaction were mixed to prepare NMR samples. $0.1 \text{ mL } 6 \text{ mM}$ Dimethylsulfoxide (DMSO) was added into the NMR samples as an internal standard (ISD) for quantification. In the NMR testing process, phase correction, baseline correction, and resolution and noise adjustments were performed on the test results to

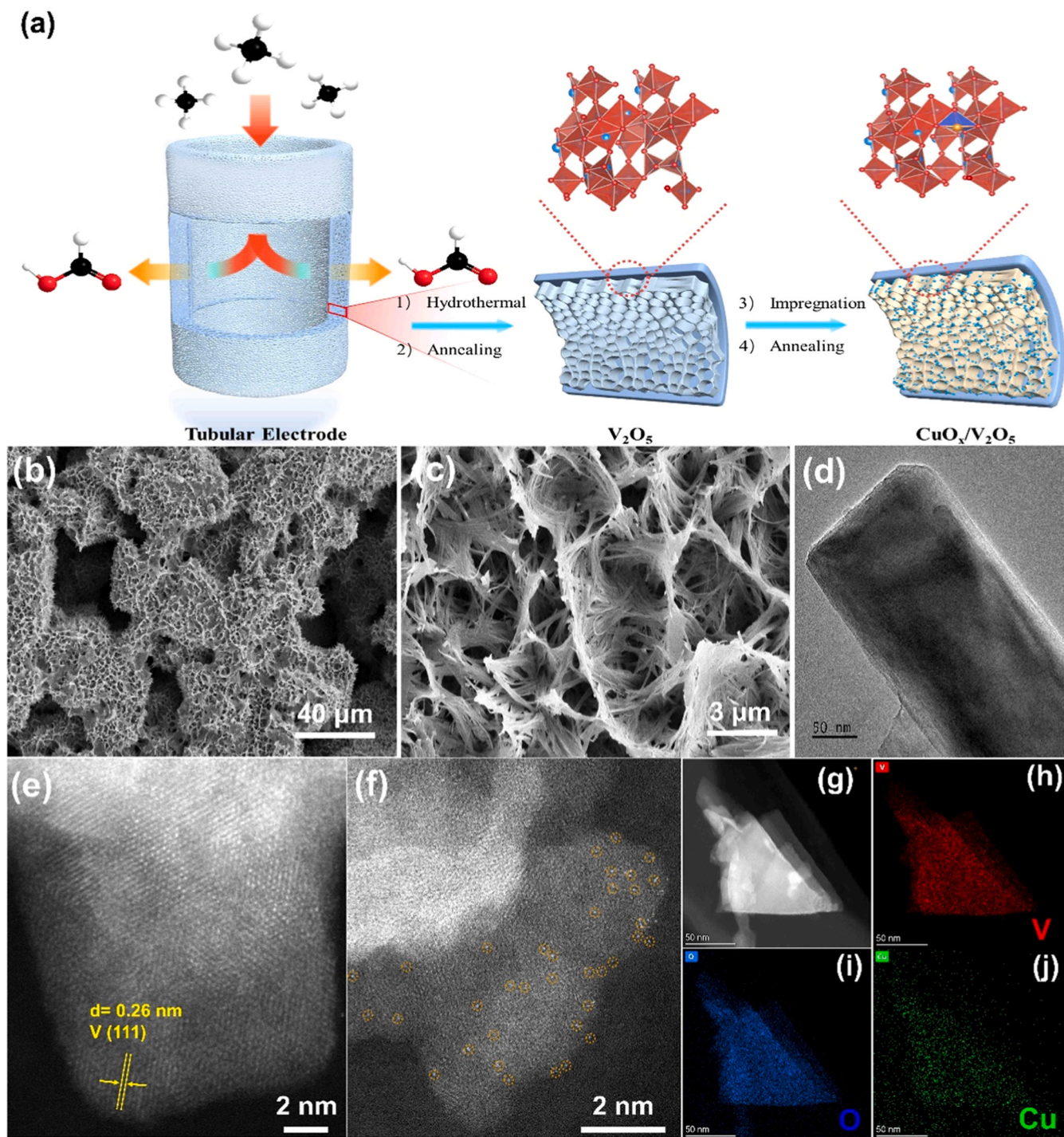


Fig. 1. (a) Schematic illustration of the tubular electrode and the synthesis process of $\text{CuO}_x/\text{V}_2\text{O}_5$ catalyst. (b) and (c) low- and high-magnification SEM images of $\text{CuO}_x/\text{V}_2\text{O}_5$. (d) TEM image and (e)-(f) high-resolution HAADF-STEM images of $\text{CuO}_x/\text{V}_2\text{O}_5$. (g)-(j) STEM image and corresponding EDS element mapping of V, O and Cu, respectively.

improve data quality.

3. Results and discussion

The tubular electrode comprises hollow porous Ti tubes and supported $\text{CuO}_x/\text{V}_2\text{O}_5$ composite catalysts, as shown in Fig. 1a. When the electrode is working, both ends of the Ti tube are sealed with glue, leaving only one CH_4 gas inlet (Figure S1). When CH_4 gas continues to enter the tube, the gas can only flow out through the hierarchically porous tube wall. As the catalyst grows in the pores on the wall, CH_4 and the catalyst will be in full contact. If the electrode is immersed in the electrolyte, a rich gas-liquid-solid three-phase reaction interface will be generated. $\text{CuO}_x/\text{V}_2\text{O}_5$ composite catalyst are in situ grown on the Ti tube support and the synthesis process can be divided into four simple steps. Firstly, the vanadium oxide (V_2O_5) with honeycomb-like porous structure was grown on the porous Ti tubes (Figure S2) by the hydrothermal method with the precursor solution containing NH_4VO_3 , $\text{H}_2\text{C}_2\text{O}_4$, and H_2O . And $\text{H}_2\text{C}_2\text{O}_4$ was added to slightly corrode the Ti substrate to improve the adhesion of V_2O_5 to the substrate. To improve the crystallinity of the V_2O_5 (Figure S3), the catalyst was calcined in an air atmosphere at 300°C for 2 h, and then was impregnated in the mixed solution containing $\text{Cu}(\text{NO}_3)_2$, $\text{C}_6\text{H}_8\text{O}_7$ and PVP to adsorb Cu^{2+} complex ions on the V_2O_5 surface. The ligand molecules $\text{C}_6\text{H}_8\text{O}_7$ and PVP play a key role to achieve the atomic-level dispersion of Cu^{2+} ions. Finally, the Cu^{2+} complex ions/ V_2O_5 composite was further calcined at 500°C for 2 h in air atmosphere to produce atomically dispersed $\text{CuO}_x/\text{V}_2\text{O}_5$ composite catalyst. The porous Ti tubes with micron scale not only serve as the growth substrate of the catalyst, but also are current collectors, forming an integrated three-dimensional (3D) $\text{CuO}_x/\text{V}_2\text{O}_5$ electrode. In order to investigate the catalytic effect of each component, pure V_2O_5 or CuO was also synthesized by a similar method on the porous Ti tubes.

The morphology of $\text{CuO}_x/\text{V}_2\text{O}_5$ catalyst was investigated by scanning/transmission electron microscopy (SEM/TEM). Compared to the pristine porous Ti substrate (Figure S4a-b), the low-magnification SEM images in Fig. 1b or Figure S5a-b show that a uniform layer of $\text{CuO}_x/\text{V}_2\text{O}_5$ composite or V_2O_5 grows on the surface and pores of the Ti substrate. The magnified SEM images (Fig. 1c) show that ultralong nanoribbons are wound into a honeycomb-like porous structure and each nanoribbon has a length of about $3\text{--}10\ \mu\text{m}$ and a width of about $150\text{--}200\ \text{nm}$. The TEM image further exhibits the ultra-thin characteristics of the nanoribbons with the thickness of about $10\text{--}20\ \text{nm}$. Interestingly, no Cu-based nanoparticles or clusters are observed in the TEM or HRTEM images (Fig. 1d), indicating the active component of Cu is very small. To further investigate the detailed structure of $\text{CuO}_x/\text{V}_2\text{O}_5$ catalyst, the high-angle annular dark-field scanning transmission electron microscopy (HAADF-STEM) was performed. As shown in Fig. 1e and f, the homogeneously dispersed bright dots are clearly observed, which corresponds to Cu single atoms species, and some Cu single atoms are distributed on the edges and tips of the nanoribbon (Figs. S6–8). At the same time, the lattice fringes of the support are observed with a planar spacing of $0.26\ \text{nm}$, indexed to the (111) crystal planes of cubic V_2O_5 [28]. Moreover, the energy-dispersive X-ray spectroscopy (EDS) element mapping reveals a homogeneous dispersion of V, O and Cu elements (Fig. 1g-j), further confirming the uniform distributions of Cu on the surface of V_2O_5 . The Cu content in $\text{CuO}_x/\text{V}_2\text{O}_5$ composite is about 2.4 at%, measured by inductively coupled plasma mass spectrometry (ICP-MS). The comparison samples of pure V_2O_5 and CuO are also characterized by SEM and TEM (Figures S5 and S9), showing the morphology of nanoribbons and nanoparticles, respectively. When Cu^{2+} was directly loaded onto Ti tube without V_2O_5 as the support, CuO nanoparticles with a diameter of about $100\ \text{nm}$ are formed on the surface of Ti tube (Figure S9c), which indicates that V_2O_5 can effectively disperse Cu ions.

The component of the $\text{CuO}_x/\text{V}_2\text{O}_5$ composite catalyst was characterized by an X-ray diffraction (XRD) pattern. The diffraction peaks of the composite are almost the same as that of pure V_2O_5 (PDF#01-086-

2248) (Fig. 2a), which belongs to the orthorhombic system (Pmmn 59) crystal type. No diffraction peaks were observed for CuO and copper vanadate compounds, but interestingly, when CuO and V_2O_5 of equal mass were uniformly mixed and calcined at 500°C for 2 h, the resulting sample exhibited clear diffraction peaks of $\text{Cu}_2\text{V}_2\text{O}_7$ (Figure S10), indicating that CuO and V_2O_5 were easily reactive. It can be inferred that the atomic level dispersed Cu^{2+} on the surface should undergo a bonding reaction with V_2O_5 at high temperatures, forming Cu-O-V bonds. However, due to the atomic level dispersed Cu^{2+} , it is not possible to form a lattice of copper vanadate. To further demonstrate the interaction between Cu^{2+} and V_2O_5 , X-ray photoelectron spectroscopy (XPS) was used to investigate the surface composition and chemical states of $\text{CuO}_x/\text{V}_2\text{O}_5$ catalyst and comparative samples. The XPS survey spectrum of $\text{CuO}_x/\text{V}_2\text{O}_5$ identifies the presence of V, Cu, and O (Figure S11), which agrees well with the EDS results. Through the V 2p spectra (Fig. 2b), it can be seen that pure V_2O_5 contains two valence state of V^{5+} at binding energies of 517.9 and $525.1\ \text{eV}$ and V^{4+} at $515.98\ \text{eV}$ and $523.38\ \text{eV}$ [28,29], respectively, among them, V^{5+} is the main component, while V^{4+} is only about 5 %. Comparison shows that the production of V^{4+} is related to the growth of V_2O_5 on the Ti substrate (Figure S12). The interaction between V_2O_5 and Ti may induce a small amount of V^{4+} . However, interestingly, for $\text{CuO}_x/\text{V}_2\text{O}_5$, there are also only the peaks of V^{5+} observed, corresponding the binding energies of 517.1 and $524.6\ \text{eV}$. The disappearance of V^{4+} and the significant shift of V^{5+} towards lower energy indicate that $\text{V}^{5+/4+}$ ions react with Cu ions and generate strong electron interactions [30]. In the comparison of the O 1s spectra of the two samples, the introduction of Cu results in a decrease in adsorbed oxygen (O_{ads}) at $531.7\ \text{eV}$ and an increase in the proportion of lattice oxygen (O_{latt}) at $530.2\ \text{eV}$ (Fig. 2b). At the same time, a significant shift of O_{latt} towards the low energy direction is also observed, possibly due to the generation of O_v . In the Cu 2p XPS spectra (Fig. 2c), compared to pure CuO , $\text{CuO}_x/\text{V}_2\text{O}_5$ exhibits two distinct characteristics: firstly, the main peak is Cu^{2+} ($934.6\ \text{eV}$), which shifts significantly towards the high-energy direction, and secondly, a small peak of Cu^+ ($931.9\ \text{eV}$) appears and the coexistence of Cu^+ species is further evidenced by the Cu LMM Auger spectra (Figure S13) with kinetic energies of $916.8\ \text{eV}$ [30,31]. A small amount of Cu^+ may be caused by the different bonding structures of V^{5+} with Cu^{2+} , just as the valence states of Cu are significantly different in different copper vanadate compounds, such as Cu^+ in CuVO_3 and Cu^{2+} in $\text{Cu}_2\text{V}_2\text{O}_7$ [30]. The shift of Cu^{2+} and the appearance of Cu^+ further prove that V^{5+} undergoes chemical reactions with $\text{Cu}^{2+}/\text{Cu}^+$ to form Cu-O-V bonds. From the results of XPS quantitative analysis, the stoichiometric ratios of V_2O_5 and $\text{CuO}_x/\text{V}_2\text{O}_5$ are about $\text{V}_2\text{O}_{4.76}$ and $\text{Cu}_{0.1}\text{V}_2\text{O}_{4.52}$, respectively, and after the loading of Cu on the surface of V_2O_5 , the stoichiometric number of O decreased, indicating the presence of O_v .

Raman spectroscopy was further used to demonstrate the formation of Cu-O-V bonds. As shown in Fig. 2d, both samples of $\text{CuO}_x/\text{V}_2\text{O}_5$ and V_2O_5 exhibit similar peaks, indicating the similar crystal structure. Interestingly, one additional peak at $895\ \text{cm}^{-1}$ was observed in the $\text{CuO}_x/\text{V}_2\text{O}_5$ composite catalyst, and this peak is consistent with one of the characteristic peaks of copper vanadate compounds (Figure S14), corresponding to Cu-O-V stretching vibration [30–32]. The formation of Cu-O-V bonds on the surface inevitably leads to changes in the lattice structure of V_2O_5 . In order to further characterize this change, EPR analysis was conducted. As shown in Fig. 2e, $\text{CuO}_x/\text{V}_2\text{O}_5$ exhibits a stronger EPR signal at around $g = 2.002$, while the signal of V_2O_5 is very weak, indicating that rich O_v are induced by atomically dispersed CuO_x in V_2O_5 [33]. As well-known, O_v will induce solid acid sites, so NH_3 -TPD analysis was used to characterize the acidity change of the catalyst. As shown in Fig. 2d, the CuO has almost no acidity, and V_2O_5 shows a desorption peak at the weak acid center ($<300^\circ\text{C}$), while $\text{CuO}_x/\text{V}_2\text{O}_5$ shows two desorption peaks at the weak acid center and strong acid center ($>300^\circ\text{C}$) (mainly Lewis acid sites). The strong Lewis acid sites are essential to adsorb and activate C-H of alkanes by proton abstraction [34]. To further demonstrate the interaction between $\text{CuO}_x/\text{V}_2\text{O}_5$ and

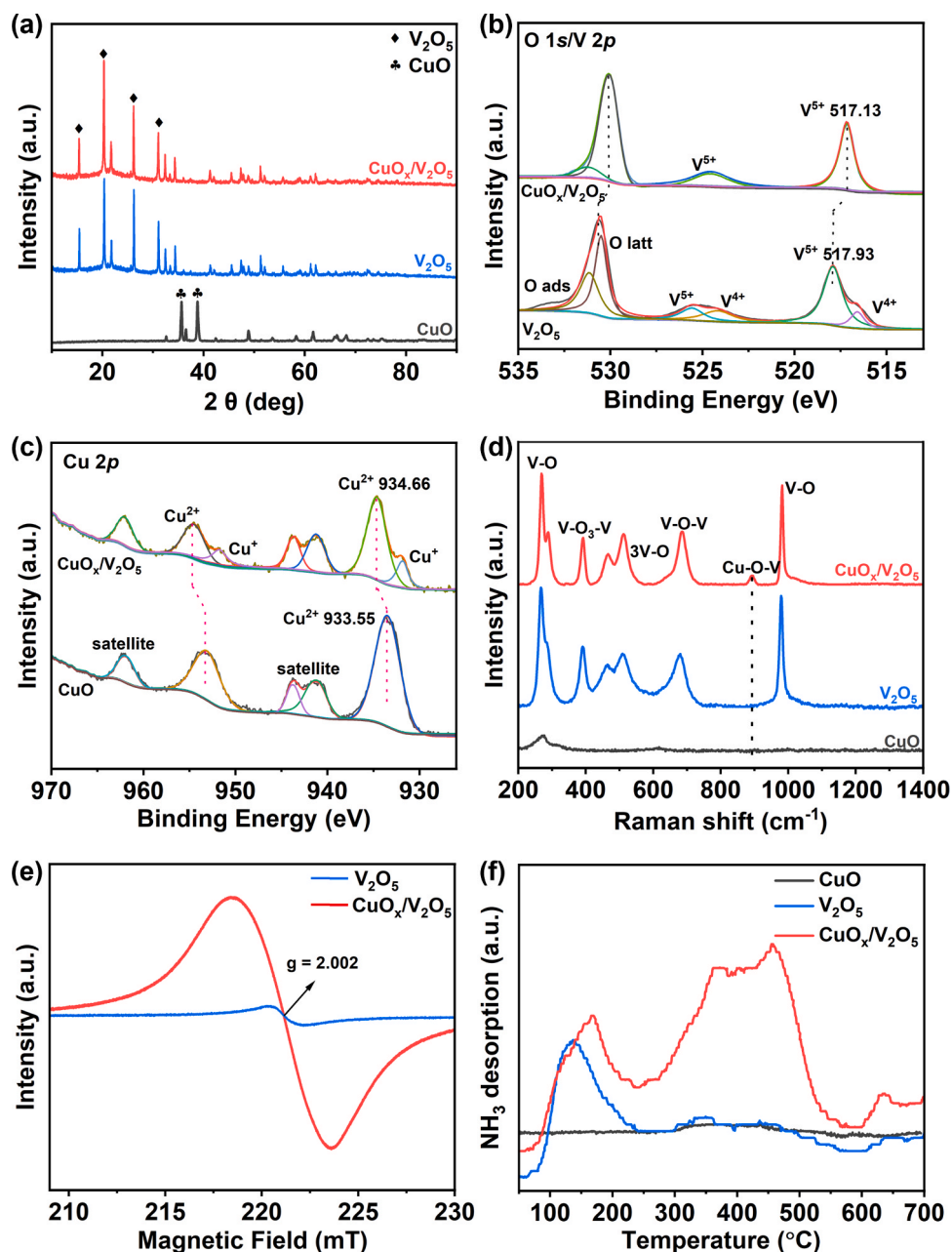


Fig. 2. (a) XRD patterns, (b) O 1s/V 2p XPS spectra, (c) Cu 2p spectra, and (d) Raman spectra of CuO, V₂O₅ and CuO_x/V₂O₅. (e) EPR spectra for O_v of V₂O₅ and CuO_x/V₂O₅. (f) NH₃-TPD curves of CuO, V₂O₅ and CuO_x/V₂O₅.

CH₄, the CH₄ adsorption capacity of the catalyst was tested. As shown in Figure S15, compared to CuO and V₂O₅, CuO_x/V₂O₅ exhibits stronger CH₄ adsorption, indicating that the strong Lewis acid sites significantly enhances the CH₄ adsorption capacity, which will play an important role in promoting the activity of eMOR [35].

To explore more detailed structural information, the samples are further investigated by X-ray absorption fine structure spectroscopy (XAFS) (Figure S16–19). Fig. 3a and b show the X-ray absorption near-edge structure (XANES) spectra of Cu and V. In the Cu K-edge spectra, the absorption edge of CuO_x/V₂O₅ locates between Cu foil and CuO indicates the averaged valence state of Cu species in CuO_x/V₂O₅ between 0 and +2 (Fig. 3a), which is consistent with XPS data. For the V K-edge spectra, strong pre-edge peaks at 5470 eV are observed in CuO_x/V₂O₅ and V₂O₅ (Fig. 3b), indicating an octahedral geometry distortion around V atoms [36–38]. It can be seen that the pre-edge peak of CuO_x/V₂O₅ shift towards lower binding energies compared to V₂O₅,

indicating a bonding effect between Cu and V. Moreover, to obtain more information about coordination and symmetry, the extended X-ray absorption fine structure (EXAFS) of the Cu and V K-edges of CuO_x/V₂O₅ are analyzed (Fig. 3c–d and Figure S16–19). As shown in Fig. 3c, CuO_x/V₂O₅ shows an intensity contribution at 1.43 Å, corresponding to Cu–O coordination. The fitted data are shown in Table S1, and the Cu–O coordination number of CuO_x/V₂O₅ is ~3.2, which means that the average value of x in the CuO_x complex is about 3.2, while in CuO, the Cu–O coordination number is ~4.0. Interestingly, for the second shell coordination of Cu–O–Cu species, in CuO, it appears at 2.8 Å, while in CuO_x/V₂O₅, it appears at 2.6 Å, moreover, their coordination numbers are completely different, with the former being ~4.0 and the latter being ~1.4, indicating that the structure of CuO_x in CuO_x/V₂O₅ is different from that of CuO, not CuO nanoclusters or particles. As observed in the HAADF-STEM images in Fig. 1f and S8, a large amount of atomic level Cu is continuously distributed at the edge of V₂O₅ nanosheets, so these

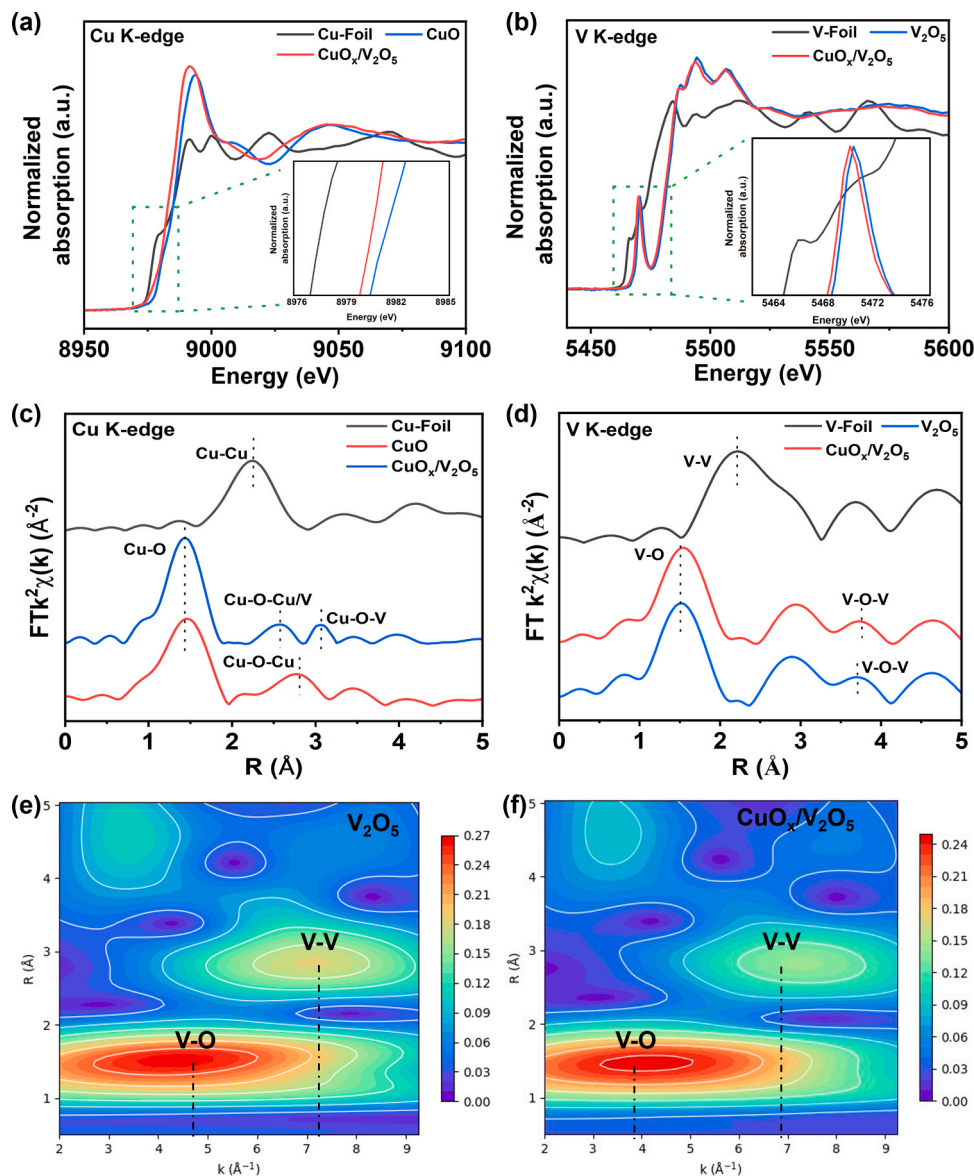


Fig. 3. (a) XANES spectra of Cu K-edge of Cu-foil, CuO and CuO_x/V₂O₅, (b) XANES spectra of V K-edge of V-foil, V₂O₅ and CuO_x/V₂O₅, (c) EXAFS spectra of Cu K-edge of Cu-foil, CuO and CuO_x/V₂O₅, (d) EXAFS spectra of V K-edge of V-foil, V₂O₅ and CuO_x/V₂O₅, (e) and (f) WT-EXAFS contour plots of V₂O₅ and CuO_x/V₂O₅.

continuously distributed CuO_x form a small amount of Cu-O-Cu bonds. At the same time, CuO_x/V₂O₅ exhibits a significant Cu-O-V coordination contribution, with coordination numbers of ~ 0.6 and ~ 0.8 at 2.7 Å and 3.2 Å, respectively, which is significantly different from copper vanadate (Table S1). This further indicates the formation of Cu-O-V bonds but not copper vanadate compounds. In Fig. 3d and Table S2, the slightly elongated distance of V-O and V-V bonds in CuO_x/V₂O₅ is observed compared with the V₂O₅ due to the formation of Cu-O-V bonds. Moreover, wavelet transform (WT)-EXAFS is also used to determine the metal-O and metal-metal paths (Fig. 3e and f), and the WT plots of the V K-edge data in V₂O₅ and CuO_x/V₂O₅ are compared to explore the relationship between Cu and V. A maximum at the center point of $R \approx 2.8$ Å and $k \approx 7$ Å⁻¹ in V₂O₅ EXAFS WT pattern of V K-edge correspond to multiple scattering paths of V-O-V bonding. Interestingly, the CuO_x/V₂O₅ pattern on the R-space 2.7 Å corresponds to a relatively bigger scattering ($k = 7.5$ Å⁻¹), further illustrating the strong interaction between Cu and V [38].

The catalytic performance of CuO_x/V₂O₅ toward eMOR was investigated in a neutral electrolyte with a standard three-electrode system, in which the tubular electrode was used directly as the working electrode.

Fig. 4a shows linear sweep voltammetry (LSV) curves of CuO_x/V₂O₅ in 0.1 M Na₂SO₄ aqueous solutions saturated with N₂ or CH₄, respectively. Obviously, compared to the current density in N₂, the current density significantly increases after introducing CH₄, indicating that CuO_x/V₂O₅ has a higher activity for CH₄ oxidation. At a current density of 10 mA cm⁻², the potential of oxygen evolution reaction (OER) in N₂ is 2.69 V vs. reversible hydrogen electrode (RHE), while in CH₄, the reaction potential drops to 2.51 V vs. RHE, a significant decrease by 180 mV in comparison to OER, indicating that the CH₄ oxidation reaction occurs preferentially, which effectively suppresses OER side reactions. To investigate the effect of potential on the selectivity of electrochemical oxidative CH₄, a series of long-term chronoamperometry at various potentials are carried out with CH₄. It is found that when the working potential is less than 2.2 V vs. RHE, no product can be collected (Figure S20). So, the potential range is chosen from 2.2 to 3.2 V vs. RHE, and the results show that the FE and current density of FA increase continuously and reach the maximum values at 2.6 V vs. RHE, corresponding to 92 % and 14.4 mA cm⁻² with a very small amount of O₂ and CO₂ production (Fig. 4b, and Figure S21), respectively. Moreover, the concentration of FA can reach 17.5 mM

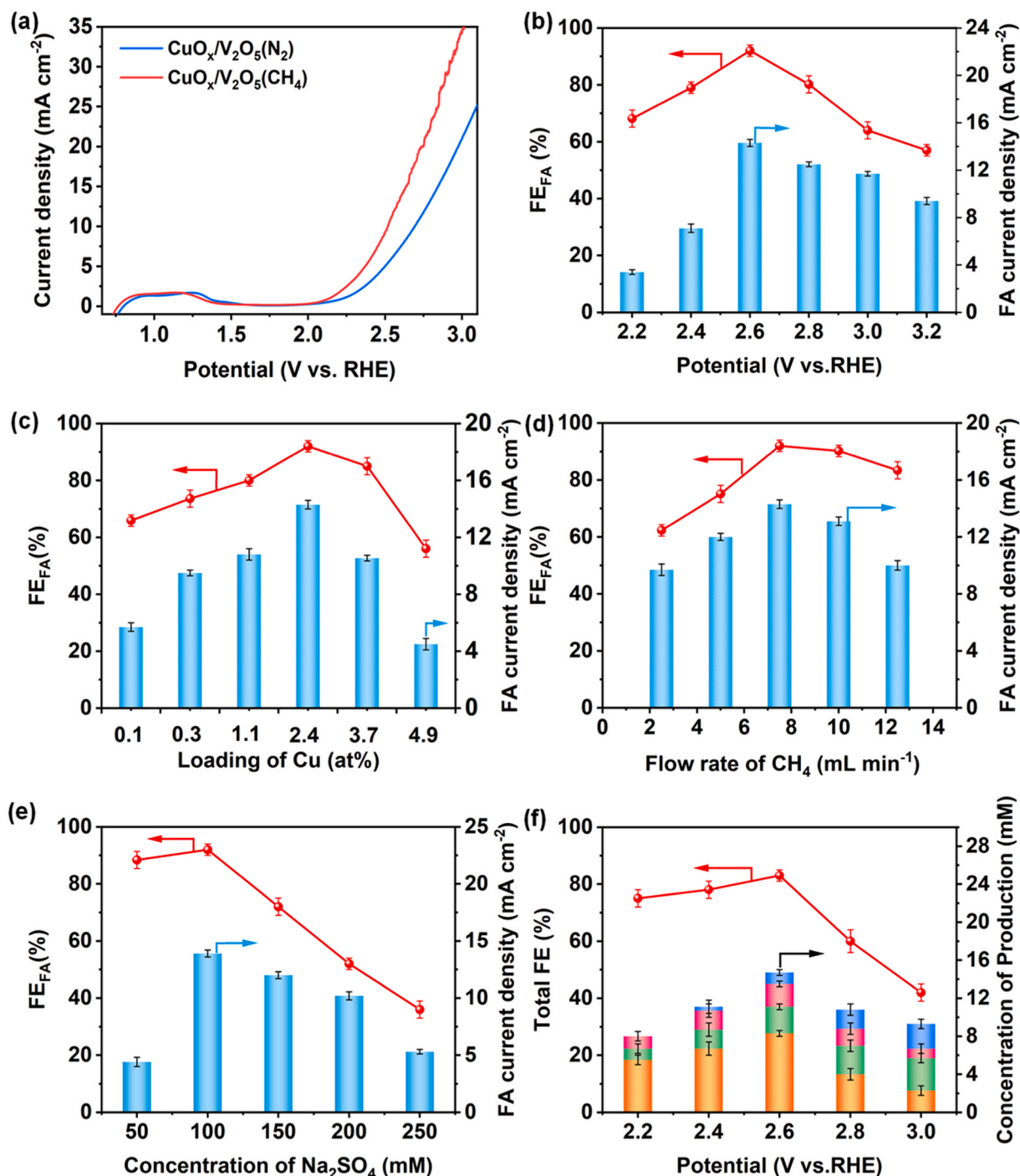


Fig. 4. (a) LSV curves of the $\text{CuO}_x/\text{V}_2\text{O}_5$ anode at a scan rate of 10 mVs^{-1} in 0.1 M Na_2SO_4 electrolyte saturated with N_2 or CH_4 . (b)–(e) FE and current density of FA at different potentials (b), loading amount of Cu (c), flow rate of CH_4 (d) and concentration of Na_2SO_4 (e). (f) Total FE and concentration of products in 0.1 M Na_2CO_3 electrolyte on the $\text{CuO}_x/\text{V}_2\text{O}_5$ catalyst.

(Figure S22a). When the potential further increases, FE and current density of FA begin to decrease, and at 3.2 V vs. RHE, they decrease to about 57 % and 9.2 mA cm^{-2} , respectively. And the change in FA concentration is consistent with the change in current density. The gaseous and liquid products are analyzed through gas chromatography (GC), high-performance liquid chromatography (HPLC) and nuclear magnetic resonance (NMR) after the reaction (Figure S23), and the results show that there is only FA and no other products, which indicates that this oxidation reaction has good product selectivity.

In order to explore the influencing factors of performance, we

systematically investigated the effects of Cu loading, CH_4 gas flow rate, electrolyte concentration, and electrolyte type on performance. Fig. 4c and Figure S22b shows the variation of FE, current density and concentration of FA with the concentration of $\text{Cu}(\text{NO}_3)_2$ in the impregnation solution, indirectly reflecting the effect of Cu loading on performance. It can be seen that the FE and current density of FA almost linearly increase with the Cu loading, indicating that the number of active sites of atomically dispersed Cu determines the amount of FA produced. When the loading amount of Cu reaches 2.4 at%, the performance reaches its highest, and as the loading amount continues to increase, the activity

begins to decrease, with FE of FA decreasing to 85 % at 3.7 at% and 56 % at 4.9 at%. The TEM image shows that the sample with a loading of 4.9 at% generates obvious 1–3 nm CuO nanoparticles (Figure S24), indicating that the activity of the CuO nanoparticles is much lower than that of atomically dispersed CuO_x. The flow rate of CH₄ also has a certain impact on performance (Fig. 4d and Figure S22c). A low flow rate leads to insufficient gas reaching the catalyst surface, while a high flow rate may blow away the electrolyte on the catalyst surface. So, as shown in Fig. 4d, the performance first increases and then decreases with the CH₄ flow rate, reaching its highest value when the flow rate is 7.5 mL min⁻¹. In addition to the above two factors, the concentration and type of electrolyte also play a crucial role in the reaction process. From Fig. 4e and Figure S22d, it can be seen that when the concentration of Na₂SO₄ is reduced by half (50 mM), the current density of FA decreases seriously, less than one-third of the highest value, while FE is very high (88.4 %), close to the highest value. The low-concentration Na₂SO₄ solution has poor ion conductivity, leading to the very low current density. On the

contrary, when the concentration of Na₂SO₄ is higher than the optimal value (100 mM) and continues to increase, the performance almost linearly decreases, while the OER activity significantly increases. The high concentration of Na₂SO₄ increases the current density, but its performance decreases instead of increasing. This may be due to two reasons: firstly, the enhanced OER activity in high concentration of Na₂SO₄, and secondly, the quenching of free radicals by high concentration of SO₄²⁻ reduces the concentration of free radicals that oxidize CH₄. At the same time, the type of electrolyte determines the type of product. For example, if Na₂SO₄ is replaced with Na₂CO₃, the product will become a mixture of HCOOH, CH₃COOH, and CH₃OH (Fig. 4f and Figure S22f), leading to a serious decrease in selectivity. Different types of electrolyte anions will induce the production of different active free radicals, leading to the production of different products. Therefore, for the oxidation of CH₄ to FA, the highly active reaction interface is based on the synergy of multiple factors, including the optimized number of active sites, the appropriate electrolyte type and concentration, and the

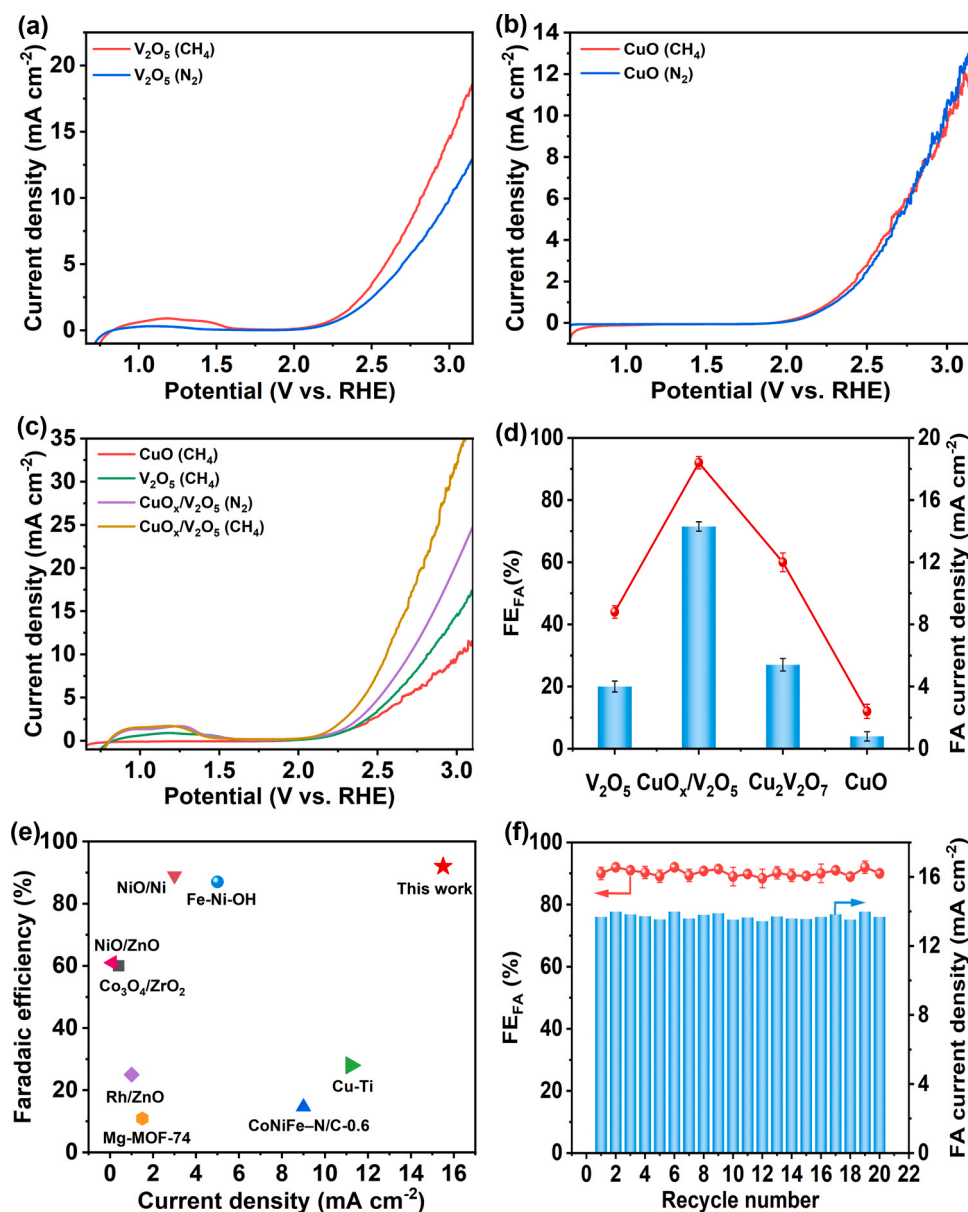


Fig. 5. (a) and (b) LSV curves on V₂O₅ and CuO catalysts in 0.1 M Na₂SO₄ electrolyte saturated with N₂ or CH₄ at 10 mV s⁻¹. (c) LSV curves on the three catalysts of CuO, V₂O₅ and CuO_x/V₂O₅ in CH₄-saturated 0.1 M Na₂SO₄ electrolyte at 10 mV s⁻¹. (d) Comparison of maximum FE and current density of FA on different catalysts. (e) Comparison of catalytic performances between the CuO_x/V₂O₅ system in this work and other oxidation systems reported in the literature (Reactions occur at room temperature and atmospheric pressure). (f) Stability test on the CuO_x/V₂O₅ catalyst.

appropriate gas flow rate.

In order to investigate the contribution of each component to activity in $\text{CuO}_x/\text{V}_2\text{O}_5$, the performances of pure V_2O_5 and CuO were also tested for comparison. The LSV curves of each catalyst are compared in CH_4 and N_2 saturated electrolytes, and it is found that the introduction of CH_4 significantly increases the current density in V_2O_5 , indicating that V_2O_5 has a certain adsorption and activation ability for CH_4 (Fig. 5a). However, in CuO , the two curves of CH_4 and N_2 almost overlap, indicating that the adsorption ability of Cu sites for CH_4 is weak, but they have a certain H_2O oxidation ability (Fig. 5b). To compare the activity of V_2O_5 , CuO , and $\text{CuO}_x/\text{V}_2\text{O}_5$, Fig. 5c shows the LSV curves of the three catalysts in CH_4 saturated electrolytes and it can be seen that the oxidation current density of V_2O_5 is slightly higher than that of CuO , but both are significantly lower than that of $\text{CuO}_x/\text{V}_2\text{O}_5$. The LSV curve of $\text{CuO}_x/\text{V}_2\text{O}_5$ in N_2 saturated electrolyte is also added in Fig. 5c, interestingly, although its current density is significantly lower than that of $\text{CuO}_x/\text{V}_2\text{O}_5$ in CH_4 saturated electrolyte, it is obviously higher than that of V_2O_5 and CuO under CH_4 saturated electrolytes, which indicates that atomically dispersed CuO_x can promote H_2O oxidation in the absence of CH_4 . Figure S15 has demonstrated the difference in the adsorption capacity of three catalysts for CH_4 , with $\text{CuO}_x/\text{V}_2\text{O}_5$, V_2O_5 , and CuO decreasing sequentially. At the same time, the changes in current density with CH_4 adsorption and desorption in the non-Faraday reaction region also reflect the same trend of the three catalysts (Figure S25) [39]. Combining Fig. 5a, Figure S15, and Figure S25, it can be seen that the adsorption capacity of the catalyst for CH_4 determines the magnitude of the oxidation current density in LSV curves, and $\text{CuO}_x/\text{V}_2\text{O}_5$ exhibits the strongest CH_4 adsorption, resulting in the highest oxidation current, followed by V_2O_5 and CuO . The difference in performance between V_2O_5 and CuO is further reflected by the FE and concentration of the product FA, as shown in Fig. 5d and Figure S22e. In the V_2O_5 sample, the maximum FE of FA is 44 % at the current density of 4.2 mA cm^{-2} , and the maximum concentration reaches 5.0 mM, while in CuO , the maximum FE of FA is only 12 % at 1.0 mA cm^{-2} and the maximum concentration is 0.8 mM, the former is almost four times higher than the latter. Comparing the performance of $\text{CuO}_x/\text{V}_2\text{O}_5$ (FE: 92 %, current density: 14.4 mA cm^{-2} and FA concentration: 17.5 mM), it can be seen that the sum of pure V_2O_5 and CuO performance is much lower than that of $\text{CuO}_x/\text{V}_2\text{O}_5$, indicating that the combination of atomically dispersed CuO_x and V_2O_5 creates a synergistic catalytic system. We also tested the eMOR performance of a copper vanadate compound ($\text{Cu}_2\text{V}_2\text{O}_7$), and maximum FE of FA is only 60 % at the current density of 5.4 mA cm^{-2} (Fig. 5d), much lower than $\text{CuO}_x/\text{V}_2\text{O}_5$, indicating two different active sites. It is worth emphasizing that the current density and FE achieved by the $\text{CuO}_x/\text{V}_2\text{O}_5$ catalyst under ambient condition exceed most reported results of traditional electrooxidation systems (Fig. 5e and Table S4), which proves the advantages of $\text{CuO}_x/\text{V}_2\text{O}_5$ catalyst and its reaction interface with Na_2SO_4 . In addition to high activity, the $\text{CuO}_x/\text{V}_2\text{O}_5$ catalyst also shows good stability. After 20 cycles of use, the FE and concentration of FA show little change (Fig. 5f and Figure S26). This above data indicated that the catalyst of $\text{CuO}_x/\text{V}_2\text{O}_5$ has excellent stability. Interestingly, even when CH_4 gas is significantly diluted, the $\text{CuO}_x/\text{V}_2\text{O}_5$ catalyst still exhibits high activity for FA production (Figure S27). However, if the reactant of CH_4 does not pass through the tubular electrode, there is no FA or other products. To further track the carbon path in the eMOR, we conducted ^{13}C isotope-tracing experiments on $^{13}\text{CH}_4$ (Figure S28) and the NMR and GC-MS test results indicate that the C source of FA comes from CH_4 .

The electrochemical surface areas (ECSA) and electrochemical impedance spectra (EIS) tests of three catalysts are performed to further explain the high activity of $\text{CuO}_x/\text{V}_2\text{O}_5$. The calculated ECSA of CuO , V_2O_5 and $\text{CuO}_x/\text{V}_2\text{O}_5$ are 21, 24, and 62 cm^2 (Figure S29), respectively, suggesting that $\text{CuO}_x/\text{V}_2\text{O}_5$ exposes more active sites. The EIS data are fitted using the equivalent circuit, where R_s (high frequencies) and R_{ct} (lower frequencies) are associated with the internal Ohmic resistance of the bulk membrane and charge transfer resistance at the electrolyte/

membrane interface, respectively. R_s highly correlates with the electrical conductivity of the membrane electrode, which is contributed by both bulk and surface O_v . Compared with CuO and V_2O_5 , the R_s of $\text{CuO}_x/\text{V}_2\text{O}_5$ are only $5.09\text{E-}6$ (Figure S30 and Table S3). Moreover, the EIS reveal that the charge-transfer resistance (R_{ct}) of $\text{CuO}_x/\text{V}_2\text{O}_5$ is 11.73Ω , which is lower than that of V_2O_5 (13.45Ω) and CuO (15.45Ω) (Figure S30 and Table S3), implying that the fast electron-transfer process to reduce the Schottky barriers at both catalyst-electrolyte and catalyst-electrode interfaces. From the smaller R_{ct} data than V_2O_5 and CuO , $\text{CuO}_x/\text{V}_2\text{O}_5$ can ascribe to the accelerated carriers transfer mobility through the unique Cu-O-V . In addition, as shown in Figure S31, the $\text{CuO}_x/\text{V}_2\text{O}_5$ has a similar trend in the Bode plots for V_2O_5 and CuO , however, its phase angle values are much higher than that of V_2O_5 and CuO , which also illustrates the faster reaction rate.

In order to investigate the changes in the sample during the catalytic reaction process, $\text{CuO}_x/\text{V}_2\text{O}_5$ sample after performance testing was systematically characterized. As shown in Fig. 6a, the SEM image shows that the honeycomb shaped morphology formed by wrapping ultra-long nanoribbons is well maintained on the Ti tubular electrode. In Fig. 6b, the HRTEM image shows that there are no obvious cluster or particles on the surface of the nanoribbons, indicating that CuO_x species remain highly dispersed. In addition, the EDS mapping shows that the elements of Cu, V and O are uniformly distributed throughout the nanoribbon (Fig. 6d-f). The comparisons of XRD patterns and XPS spectra before and after the electrochemical oxidation of CH_4 show that there is no significant change in the $\text{CuO}_x/\text{V}_2\text{O}_5$ catalyst (Figure S32 and Fig. 6g-h), V still maintains a high valence state of +5, and Cu still exists as Cu^+ and Cu^{2+} . The Raman spectra further confirm that the characteristic peak of the Cu-O-V bond still exists in $\text{CuO}_x/\text{V}_2\text{O}_5$ (Fig. 6i). However, the EPR spectra (Fig. 6j) show a slight decrease in the EPR signal at around $g = 2.002$ after the reaction, indicating a decrease in O_v . Meanwhile, the EXAFS spectra (Fig. 6k-l and Table S1-2) show that the bond lengths of Cu-O and V-O increase slightly after the reaction. This may be due to the weakening of the bond strength of Cu-O and V-O bonds on the catalyst surface during the participation of Cu and V in the electrooxidation process, which will result in a certain amount of loss of Cu and V during long-term operation, leading to a decrease in performance. So, the stability of the Cu-O-V bond determines the stability of the catalyst's activity, and selecting the appropriate potential and current may prolong the stability time of the Cu-O-V bond.

To gain insight into the mechanism for electrocatalytic oxidation of CH_4 over a $\text{CuO}_x/\text{V}_2\text{O}_5$ anode, EPR, in situ potential-dependent Raman spectroscopy and in-situ ATR-IRAS tests were carried out. Firstly, EPR analysis is conducted to identify possible radical species by using 5,5-dimethyl-1-pyrroline N-oxide (DMPO) as the spin trap agent, and the electrolyte attached to the surface of the electrode is quickly extracted. The EPR spectra of three comparative systems are shown in Fig. 7a. Before the voltage is applied, and no signal is found in the EPR spectra (Figure S33). When a voltage (2.6 V vs. RHE) is applied to the three oxidation systems, distinct DMPO-EPR quadruple signals appeared over the three catalysts of CuO , V_2O_5 and $\text{CuO}_x/\text{V}_2\text{O}_5$. The characteristic peaks of DMPO-OH ($\alpha_N = \alpha_H = 1.49 \text{ mT}$) [40,41] is exhibited in all three catalysts, indicating that all three catalysts produce surface-adsorbed $\cdot\text{OH}$ intermediate. Interestingly, the radical signal cannot be detected in the bulk solution, indicating that the $\cdot\text{OH}$ intermediate mainly adsorbs on the electrode surface. By comparison, it can be seen that the peak intensity in CuO is stronger than in V_2O_5 , indicating that Cu active sites facilitate the production of $\cdot\text{OH}$ species. In addition to $\cdot\text{OH}$, the signal of DMPO- CH_3 is also observed in V_2O_5 and $\text{CuO}_x/\text{V}_2\text{O}_5$, and the peak intensity in V_2O_5 is significantly weaker than in $\text{CuO}_x/\text{V}_2\text{O}_5$. The in-situ potential-dependent Raman spectroscopy was used to further investigate the changes in intermediates during the reaction process. As shown in Fig. 7b, for $\text{CuO}_x/\text{V}_2\text{O}_5$, the sharp peaks at 265 cm^{-1} , 517 cm^{-1} and 701 cm^{-1} assigned to V_2O_5 species appears at open-circuit potential (OCP) [42]. When a 1.6 V vs. RHE voltage is applied to the electrode, no significant changes are observed, but when

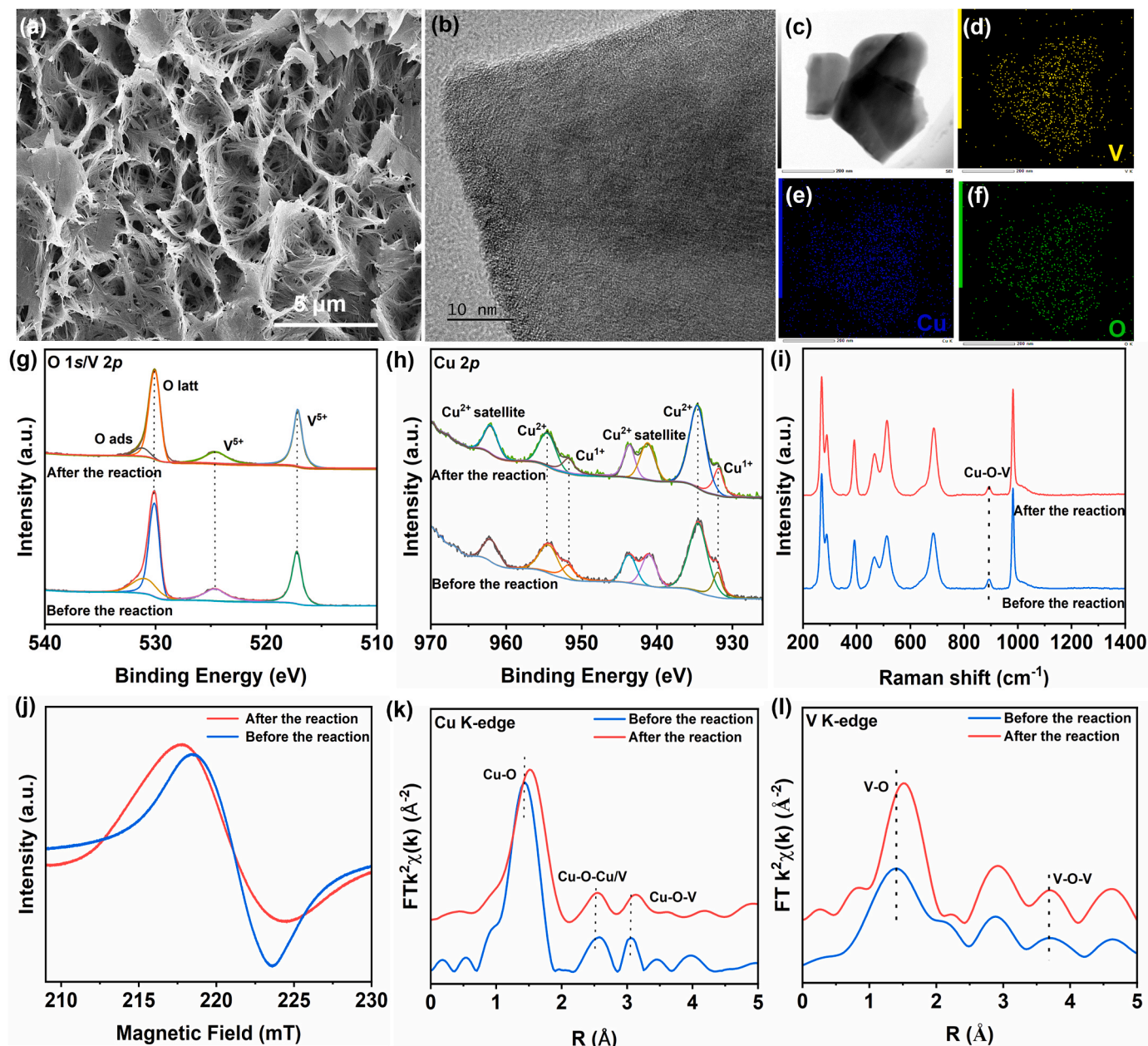


Fig. 6. (a) SEM image and (b) HRTEM image of the $\text{CuO}_x/\text{V}_2\text{O}_5$ catalyst after performance test. (c)–(f) EDS element mapping of V, Cu and O after performance test. (g) and (h) O 1s, V 2p and Cu 2p XPS spectra of $\text{CuO}_x/\text{V}_2\text{O}_5$ before and after performance test. (i) Raman spectra of $\text{CuO}_x/\text{V}_2\text{O}_5$ before and after performance test. (j) EPR spectra for O_v of $\text{CuO}_x/\text{V}_2\text{O}_5$ before and after performance test. (k) and (l) V K-edge and Cu K-edge of EXAFS spectra of $\text{CuO}_x/\text{V}_2\text{O}_5$ before and after performance test.

the voltage increases to 1.8 V vs. RHE, three new peaks appear, with peaks at 770 and 1351 cm^{-1} corresponding to $^*\text{COOH}$ and the peak at 886 cm^{-1} corresponding to $^*\text{OH}$ (Fig. 7b) [43]. Meanwhile, a weak peak at 1026 cm^{-1} was detected when the electrode potential increased to 2.0 V vs. RHE [44], which was corresponding to the $^*\text{OCH}_3$, and the peak intensity of $^*\text{OCH}_3$ quickly disappears with the increase of electrode potential. For the comparison sample V_2O_5 , the peaks of all three species have significantly weakened (Fig. 7c), indicating the weak adsorption capacity of V_2O_5 on reaction intermediates. Interestingly, in the in-situ Raman spectra of CuO (Fig. 7d), only the peaks of CuO (283 cm^{-1}), $^*\text{OH}$ (886 cm^{-1}), and SO_4^{2-} (978 cm^{-1}) [28,45] are observed, which is consistent with the EPR result. And, with the increase of electrode potential, the peak of SO_4^{2-} first increases and then decreases, which is mainly because the sulfate is adsorbed to the surface of electrode under the action of electric field at the lower potential, while

the higher potential will cause the occurrence of OER, and O_2 occupies the electrode surface thus reducing the adsorption of sulphate on the electrode surface. Fig. 7e shows the ATR-FTIR spectra collected at different electrode potentials on the $\text{CuO}_x/\text{V}_2\text{O}_5$ catalyst. In OCP, almost no absorption peaks are observed. As the applied potential increased, five peaks are observed. Among them, the four peaks at wave numbers of 1105 cm^{-1} , 1254 cm^{-1} and 1510 cm^{-1} correspond to the four reaction intermediates of $^*\text{COOH}$, $^*\text{OCH}_3$ and HCHO^* , respectively [23,46], while the two peaks at wave numbers of 1153 cm^{-1} and 1195 cm^{-1} which are assigned as C-O stretch of alkoxy and C-OH stretch of HCHO^* , respectively [47,48]. Based on the above analysis, the reaction process for the electrooxidation of CH_4 to FA is proposed with five steps (Fig. 7f): (1) $^*\text{OH}$ is in situ generation from H_2O by catalytic oxidation on atomically dispersed CuO_x active site; (2) CH_4 is adsorbed on the O_v induced Lewis acid sites and reacts with $^*\text{OH}$ to produce $^*\text{CH}_3$

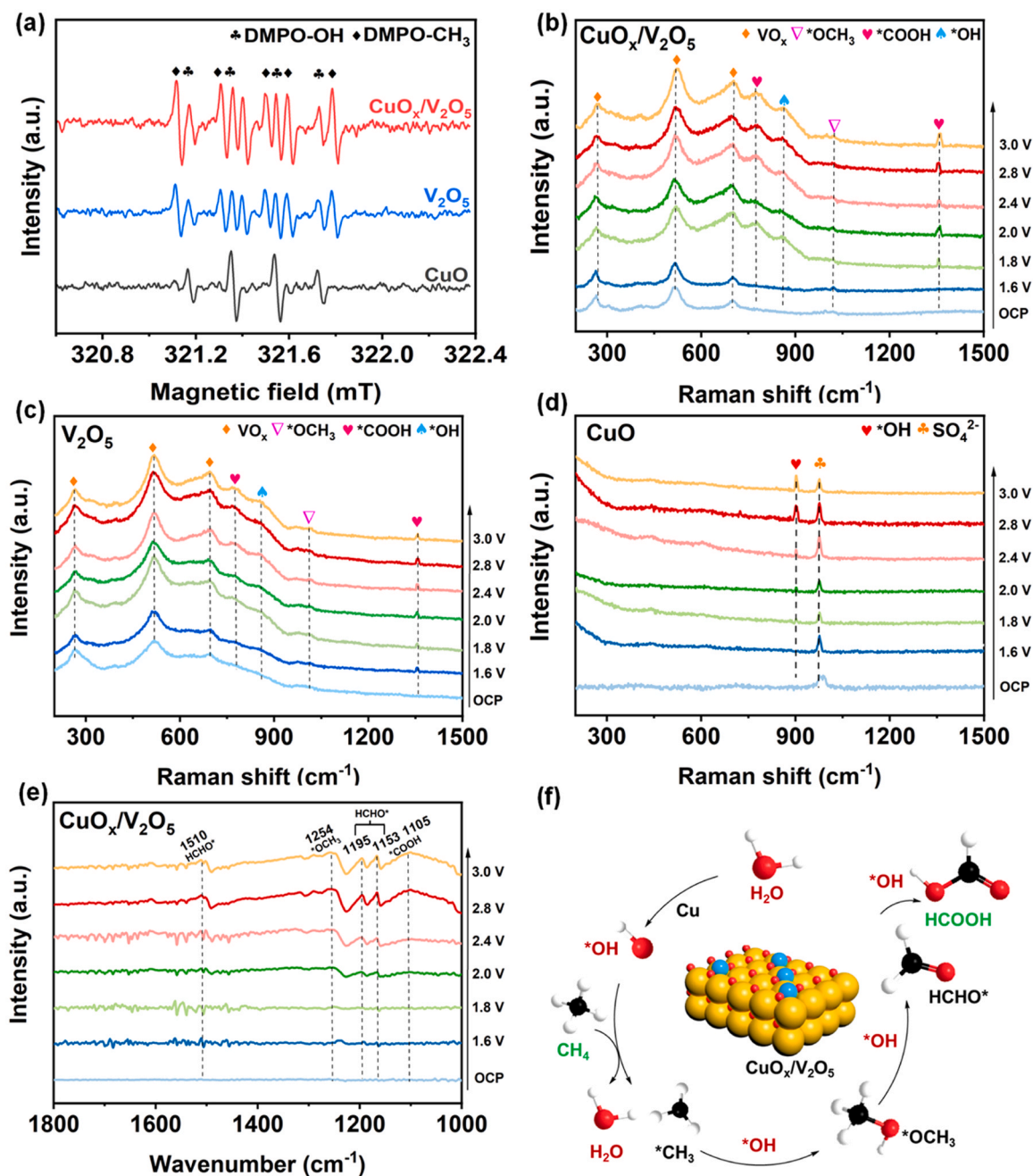


Fig. 7. (a) EPR spectra of intermediates (*OH and *CH₃) from the different oxidation systems (CuO, V₂O₅ and CuO_x/V₂O₅). (b)-(d) Potential dependent in situ Raman spectra of the different catalysts under eMOR conditions, (b) CuO_x/V₂O₅, (c) V₂O₅, and (d) CuO. (e) Potential dependent in-situ ATR-IRAS spectra on the CuO_x/V₂O₅ catalyst. (f) The proposed reaction mechanism of the direct CH₄ oxidation to FA.

intermediate; (3) The generated *CH₃ rapidly combines with *OH through rebound mechanism to generate *OCH₃; (4) *OCH₃ intermediate further reacts with *OH to produce HCHO* intermediate; (5) HCHO* intermediate further reacts with *OH to produce the final product of HCOOH. Therefore, the electrooxidation of CH₄ to FA is a multi-step free radical oxidation process.

To further understand the eMOR process, DFT calculations were performed to investigate the electronic structure and catalytic activity of V₂O₅ and CuO_x/V₂O₅. The optimized catalyst structure models are shown in Fig. 8a and S34, interestingly, the introduction of single atom Cu in the V₂O₅ model naturally generated O_v structures, which is consistent with the EPR experimental results. Fig. 8b shows the electron density difference of CuO_x/V₂O₅ and it can be seen that the electron depletion phenomenon occurs on the atomically dispersed Cu, which

will promote the atomically dispersed Cu to capture electrons from the reactant molecules and accelerate the oxidation reaction [15]. The density of states (DOS) of V₂O₅ and CuO_x/V₂O₅ are compared in Fig. 9c and d. The introduction of atomic-level Cu significantly lowers the conduction band toward the Fermi level and reduce the band gap from 2.3 eV to 1.2 eV in CuO_x/V₂O₅, which will enhance the electronic conductivity of the catalyst. Moreover, the enhanced DOS at the valence band edge near the Fermi level is observed in CuO_x/V₂O₅ compared to V₂O₅. The significant changes in the electronic structure indicate that the strong interaction between atomically dispersed CuO_x and V₂O₅. In order to explore the eMOR activity of two models, combined with in-situ test results, a comparative study was conducted on the free energy of two key reactions, the dissociation of water to generate *OH intermediates and the dissociation of CH₄ to generate *CH₃ intermediates.

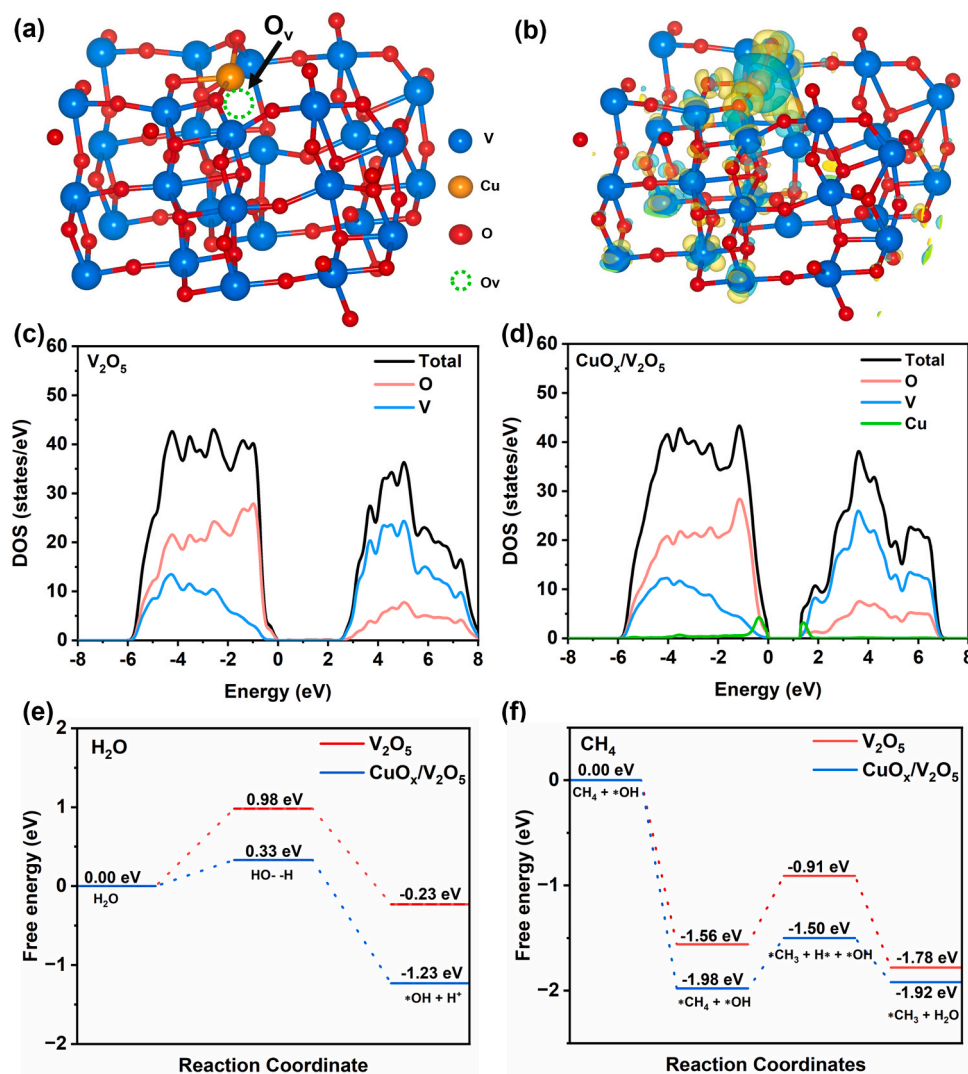


Fig. 8. (a) The catalyst model of $\text{CuO}_x/\text{V}_2\text{O}_5$. (b) Electron density difference of $\text{CuO}_x/\text{V}_2\text{O}_5$. The iso-value of the iso-surfaces is $3.0 \times 10^{-3} \text{ e} \text{ \AA}^{-3}$, and yellow (cyan) represents the charge accumulation (deletion). (c) and (d) The total and projected electron density of states (DOS) of V_2O_5 (c) and $\text{CuO}_x/\text{V}_2\text{O}_5$ (d). (e) DFT calculated adsorption free energy for H_2O dissociation on V_2O_5 and $\text{CuO}_x/\text{V}_2\text{O}_5$. (f) DFT simulated CH_4 oxidation pathway and energy profiles on V_2O_5 and $\text{CuO}_x/\text{V}_2\text{O}_5$ ($U = 0 \text{ V}$).

As shown in Fig. 8e, $\text{CuO}_x/\text{V}_2\text{O}_5$ has a smaller free energy barrier than V_2O_5 for the H_2O dissociation step (ΔG : 0.33 vs. 0.98 eV), indicating that V_2O_5 with atomically dispersed CuO_x can benefit H_2O dissociation to produce active $^*\text{OH}$. Based on the surface adsorption of $^*\text{OH}$, the CH_4 activation step is further calculated. It can be seen that in the presence of $^*\text{OH}$, even if $U=0$, the free energy of CH_4 oxidation to $^*\text{CH}_3$ is negative, indicating that the reaction proceeds spontaneously. The comparison of free energy between V_2O_5 and $\text{CuO}_x/\text{V}_2\text{O}_5$ indicates that the free energy of $\text{CuO}_x/\text{V}_2\text{O}_5$ is more negative, indicating higher activity. Once $^*\text{CH}_3$ is generated, the subsequent oxidation reaction will more easily occur spontaneously. Comparing the free energy of the two key reactions, it can be seen that the first step of producing $^*\text{OH}$ is a key step that requires energy consumption. Atomically dispersed CuO_x reduces the energy barrier and promotes the production of $^*\text{OH}$ intermediates, while the Lewis acid sites on V_2O_5 promote the adsorption of CH_4 , further reducing the free energy. The two active components synergistically oxidize CH_4 to $^*\text{CH}_3$, which is well consistent with the experimental results.

The above research proves that CH_4 can be efficiently oxidized to FA at the anode. In order to improve the efficiency of electron utilization, we further verify the coupling between cathodic CO_2 electroreduction to FA and anodic oxidation of CH_4 to FA (Fig. 9a). Bi-based materials

(metallic Bi and Bi_2O_3) have exhibited excellent activity for the CO_2 reduction reaction (CO_2RR) to produce FA, and they not only inert for HER but also beneficial for the stabilization of CO_2^* , a key intermediate for FA production. So, in this work, Bi_2O_3 grown on porous carbon tube is adopted as the cathodic catalyst for CO_2RR [49]. The morphology of the as-prepared Bi_2O_3 is investigated by SEM (Fig. 9b and Figure S35) and it can be observed that Bi_2O_3 nanosheets are uniformly grown on the carbon substrate. The diffraction peaks of the Bi_2O_3 nanosheets in the XRD pattern indicate the tetragonal system (PDF# 97–006–2979) (Inset of Fig. 9b). HRTEM image further shows the interplanar distances with the value of 0.38 nm, which agrees well with the (110) plane of cubic Bi_2O_3 (Fig. 9c). In addition, the composition and chemical characteristics of the as-prepared Bi_2O_3 are further investigated by SEM-EDS and XPS, as shown in Fig. 9(d–f) and Figure S36. Bi and O elements are evenly distributed, and Bi exhibits a +3 valence.

The electrocatalytic activity and selectivity of the Bi_2O_3 electrode for the CO_2RR are first investigated in a three-electrode system. In Fig. 9g, Bi_2O_3 exhibits a remarkable catalytic activity for the reduction of CO_2 in the 0.1 M Na_2SO_4 solution with saturated CO_2 . Fig. 9h indicates that the selectivity toward FA is dependent on the applied potential. At a potential of -0.7 V vs RHE, a maximum FE of 92 % for FA production is achieved. Based on the excellent electrocatalytic performance of $\text{CuO}_x/$

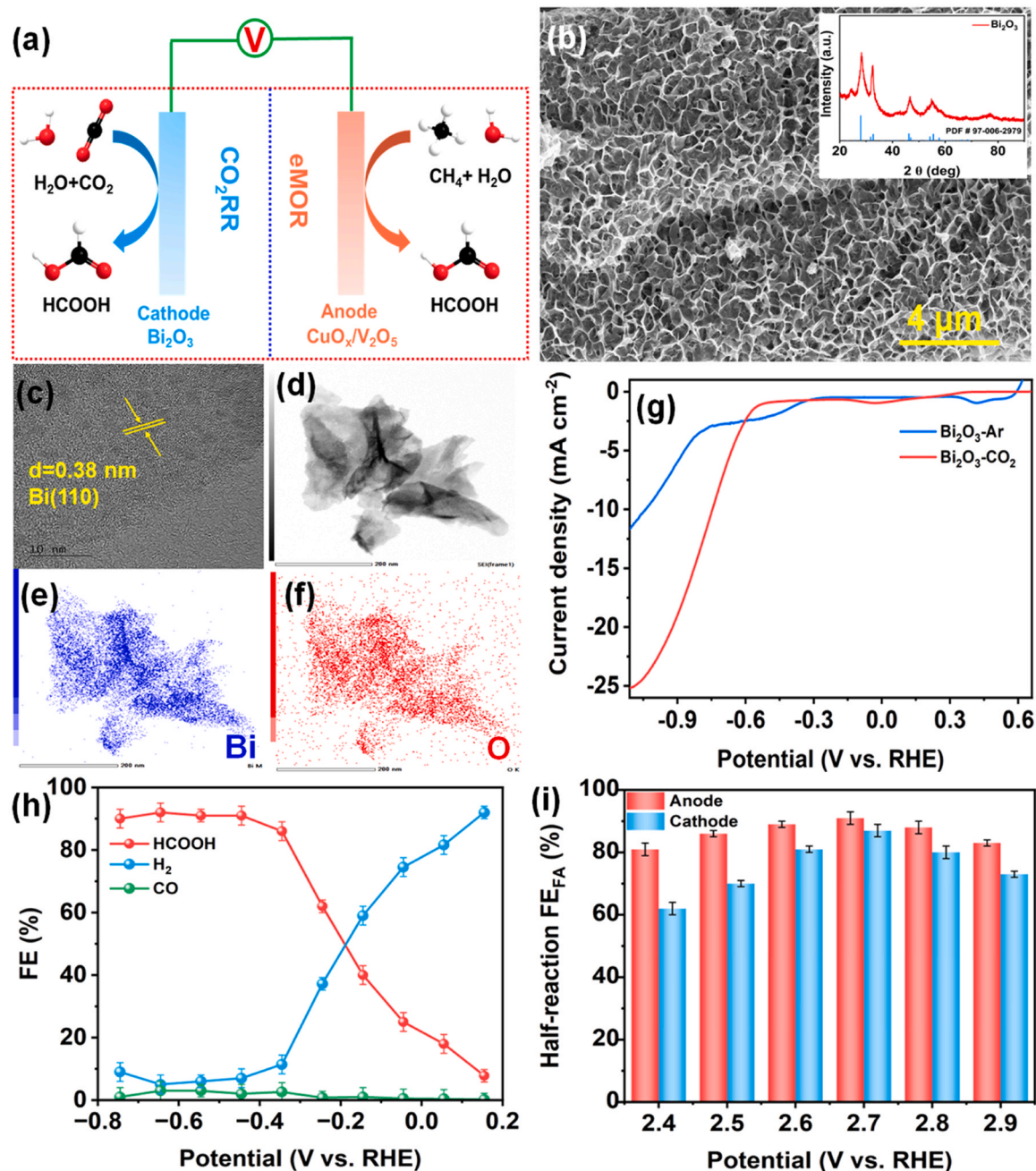


Fig. 9. (a) Schematic illustration of the two-electrode electrolyzer composing a Bi₂O₃ cathode and a CuO_x/V₂O₅ anode. (b) SEM image of the as-prepared Bi₂O₃ electrode (inset: XRD patterns of the Bi₂O₃ electrode). (c)–(f) HRTEM image of Bi₂O₃ and the corresponding elemental mapping of Bi and O. (g) LSV curves of the Bi₂O₃ electrode in Ar- or CO₂-saturated 0.1 M Na₂SO₄ solutions. (h) FEs of all products over the Bi₂O₃. (i) FEs of CuO_x/V₂O₅ for coupled eMOR and CO₂RR to produce FA at different applied potentials.

V₂O₅ for anodic eMOR and Bi₂O₃ for cathodic CO₂RR, the coupling reaction of the two is carried out in the same electrolytic cell and 0.1 M Na₂SO₄ is used as electrolyte. As expected, both anodic and cathodic reactions exhibit outstanding FEs for FA. Fig. 9i displays that the maximum FE for anodic CH₄ oxidation to FA is about 91 % at 2.7 V vs. RHE and the highest FE for CO₂RR to produce FA is 87 % at the same potential. Based on the above results, the total sum of FEs can reach 178 % for FA at 2.7 V vs. RHE by overall considering the anode and cathode reactions, which significantly improves the efficiency of electron utilization in the production of FA. In addition, techno-economic analysis (TEA) in [supplementary material](#) indicates that the simultaneous preparation of formic acid by coupling anodic CH₄ oxidation with cathodic CO₂ reduction is feasible, compared to the currently commercialized

formic acid.

4. Conclusion

In summary, we synthesize atomically dispersed CuO_x/V₂O₅ composite catalysts on hollow porous Ti tubes for selective electrooxidation of CH₄ to FA. Atomic level dispersion of Cu²⁺ ions supported on V₂O₅ is achieved under the dispersion and complexation of polyvinylpyrrolidone and citric acid. During the heat treatment process, Cu ions react with O ions to produce atomically dispersed CuO_x active sites, which simultaneously induces the generation of abundant O_v with strong Lewis acid activity. Moreover, the porous tubular electrode realizes the directional transmission of CH₄ gas in the pores and create rich

solid-liquid-gas three-phase reaction interfaces. Based on the advantages of active components and electrode structure, the optimized catalyst achieves the Faradaic efficiency of FA up to 92 % at the current density of 14.4 mA cm⁻² in the Na₂SO₄ electrolyte at ambient conditions. The mechanism research indicates that atomically dispersed CuO_x and its induced Lewis acid sites on V₂O₅ promote the electrooxidation of H₂O and the adsorption-activation of CH₄ to produce two key intermediates *OH and *CH₃. DFT calculations exhibit an obviously electron transfer behavior from atomically dispersed CuO_x to V₂O₅, which not only improves the conductivity of CuO_x/V₂O₅, but also reduces the reaction free energies of H₂O dissociation and CH₄ activation. As a proof of concept, the coupling of CH₄ electrooxidation and CO₂ electroreduction is verified by using CuO_x/V₂O₅ and Bi₂O₃ as the anodic and cathodic electrocatalysts, respectively, and realizes the simultaneous generation of FA at the anode and cathode. These findings provide valuable insights into the activation mechanism of CH₄ oxidation under mild conditions and open up perspectives for designing highly efficient single-atom catalysts for the selective activation of C-H bonds.

CRedit authorship contribution statement

Han Jiao: Software. **Tong-Tong Gao:** Methodology. **Zi-Yang Zhang:** Methodology. **Hui Fang:** Investigation. **Hao Tian:** Investigation, Data curation. **Lei Bian:** Writing – review & editing. **Zhong-Li Wang:** Writing – review & editing, Supervision, Conceptualization. **Jie-Tian Yang:** Validation.

Declaration of Competing Interest

The authors declare that they have no known competing financial interests or personal relationships that could have appeared to influence the work reported in this paper.

Data availability

Data will be made available on request.

Acknowledgments

This work is supported by the National Natural Science Foundation of China (NSFC) [grant number 22075201] and the National Key Research and Development Program of China [2022YFB4101800].

Appendix A. Supplementary material

Supplementary data associated with this article can be found in the online version at doi:10.1016/j.apcatb.2024.124001.

References

- [1] E. McFarland, Unconventional chemistry for unconventional natural gas, *Science* 338 (2012) 340–342, <https://doi.org/10.1126/science.1226840>.
- [2] B.G. Hashiguchi, M.M. Konnick, S.M. Bischof, S.J. Gustafson, D. Devarajan, N. Gunsalus, D.H. Ess, R.A. Periana, Main-group compounds selectively oxidize mixtures of methane, ethane, and propane to alcohol esters, *Science* 343 (2014) 1232–1237, <https://doi.org/10.1126/science.1249357>.
- [3] A.A. Latimer, A. Kakekhan, A.R. Kulkarni, J.K. Nørskov, Direct methane to methanol: the selectivity-conversion limit and design strategies, *ACS Catal.* 8 (2018) 6894–6907, <https://doi.org/10.1021/acscatal.8b00220>.
- [4] S. Hu, S. Ge, H. Liu, X. Kang, Q. Yu, B. Liu, Low-dimensional electrocatalysts for acidic oxygen evolution: intrinsic activity, high current density operation, and long-term stability, *Adv. Funct. Mater.* 32 (2022) 2201726, <https://doi.org/10.1002/adfm.202201726>.
- [5] Z.Y. Zhang, H. Tian, L. Bian, S.Z. Liu, Y. Liu, Z.L. Wang, Cu-Zn-based alloy/oxide interfaces for enhanced electroreduction of CO₂ to C₂₊ products, *J. Energy Chem.* 83 (2023) 90–97, <https://doi.org/10.1016/j.ijechem.2023.04.034>.
- [6] S. Xie, S. Lin, Q. Zhang, Z. Tian, Y. Wang, Selective electrocatalytic conversion of methane to fuels and chemicals, *J. Energy Chem.* 27 (2018) 1629–1636, <https://doi.org/10.1016/j.ijechem.2018.03.015>.
- [7] M.S.A.S. Shah, C. Oh, H. Park, Y.J. Hwang, M. Ma, J.H. Park, Catalytic oxidation of methane to oxygenated products: recent advancements and prospects for electrocatalytic and photocatalytic conversion at low temperatures, *Adv. Sci.* 7 (2020) 2001946, <https://doi.org/10.1002/adv.202001946>.
- [8] S. Yuan, Y. Li, J. Peng, Y.M. Questell-Santiago, K. Akkijaru, L. Giordano, D. Zheng, S. Bagi, Y. Román-Leshkov, Y. Shao-Horn, Conversion of methane into liquid fuels-bridging thermal catalysis with electrocatalysis, *Adv. Energy Mater.* 10 (2020) 2002154, <https://doi.org/10.1002/aenm.202002154>.
- [9] Q. Shen, C. Cao, R. Huang, L. Zhu, X. Zhou, Q. Zhang, L. Gu, W. Song, Single chromium atoms supported on titanium dioxide nanoparticles for synergic catalytic methane conversion under mild conditions, *Angew. Chem. Int. Ed.* 59 (2020) 1216–1219, <https://doi.org/10.1002/anie.201913309>.
- [10] Q. Wang, M. Kan, Q. Han, G. Zheng, Electrochemical methane conversion, *Small Struct.* 2 (2021) 2100037, <https://doi.org/10.1002/ssr.202100037>.
- [11] A.H. Bagherzadeh Mostaghimi, T.A. Al-Attas, M.G. Kibria, S. Siahrostami, A review on electrocatalytic oxidation of methane to oxygenates, *J. Mater. Chem. A* 8 (2020) 15575–15590, <https://doi.org/10.1039/d0ta03758c>.
- [12] N. Spinner, W.E. Mustain, Electrochemical methane activation and conversion to oxygenates at room temperature, *J. Electrochem. Soc.* 160 (2013) F1275–F1281, <https://doi.org/10.1149/05323.0001ecst>.
- [13] C. Oh, J. Kim, Y.J. Hwang, M. Ma, J.H. Park, Electrocatalytic methane oxidation on Co₃O₄ incorporated ZrO₂ nanotube powder, *Appl. Catal. B* 283 (2021) 119653, <https://doi.org/10.1016/j.apcatb.2020.119653>.
- [14] M. Ma, C. Oh, J. Kim, J.H. Moon, J.H. Park, Electrochemical CH₄ oxidation into acids and ketones on ZrO₂/NiCo₂O₄ quasi-solid solution nanowire catalyst, *Appl. Catal. B* 259 (2019) 118095, <https://doi.org/10.1016/j.apcatb.2019.118095>.
- [15] N. Xu, C.A. Coco, Y. Wang, T. Su, Y. Wang, L. Peng, Y. Zhang, Y. Liu, J. Qiao, X. D. Zhou, Electro-conversion of methane to alcohols on “capsule-like” binary metal oxide catalysts, *Appl. Catal. B* 282 (2021) 119572, <https://doi.org/10.1016/j.apcatb.2020.119572>.
- [16] J. Lee, J. Yang, J.H. Moon, Solar Cell-Powered Electrochemical methane-to-methanol conversion with CuO/CeO₂ catalysts, *ACS Energy Lett.* 6 (2021) 893–899, <https://doi.org/10.1021/acseenergylett.0c02553>.
- [17] C. Kim, H. Min, J. Kim, J. Sul, J. Yang, J.H. Moon, NiO/ZnO heterojunction nanorod catalyst for high-efficiency electrochemical conversion of methane, *Appl. Catal. B* 323 (2023) 122129, <https://doi.org/10.1016/j.apcatb.2022.122129>.
- [18] E. Ponticorvo, M. Iuliano, C. Cirillo, M. Sarno, Selective C₂ electrochemical synthesis from methane on modified alumina supporting single atom catalysts, *Chem. Eng. J.* 451 (2023) 139074, <https://doi.org/10.1016/j.cej.2022.139074>.
- [19] Q. Wang, T. Li, C. Yang, M. Chen, A. Guan, L. Yang, S. Li, X. Lv, Y. Wang, G. Zheng, Electrocatalytic methane oxidation greatly promoted by chlorine intermediates, *Angew. Chem. Int. Ed.* 60 (2021) 17398–17403, <https://doi.org/10.1002/anie.202105523>.
- [20] A. Prajapati, R. Sartape, N.C. Kani, J.A. Gauthier, M.R. Singh, Chloride-promoted high-rate ambient electrooxidation of methane to methanol on patterned Cu-Ti bimetallic oxides, *ACS Catal.* 12 (2022) 14321–14329, <https://doi.org/10.1021/acscatal.2c03619>.
- [21] Y. Song, Y. Zhao, G. Nan, W. Chen, Z. Guo, S. Li, Z. Tang, W. Wei, Y. Sun, Electrocatalytic oxidation of methane to ethanol via NiO/Ni interface, *Appl. Catal. B* 270 (2020) 118888, <https://doi.org/10.1016/j.apcatb.2020.118888>.
- [22] J. Li, L. Yao, D. Wu, J. King, S.S.C. Chuang, B. Liu, Z. Peng, Electrocatalytic methane oxidation to ethanol on iron-nickel hydroxide nanosheets, *Appl. Catal. B* 316 (2022) 121657, <https://doi.org/10.1016/j.apcatb.2022.121657>.
- [23] C. Kim, H. Min, J. Kim, J.H. Moon, Boosting electrochemical methane conversion by oxygen evolution reactions on Fe-N-C single atom catalysts, *Energy Environ. Sci.* 52 (2023) 3215–3264, <https://doi.org/10.1039/d3ee00027c>.
- [24] J. Jang, K. Shen, C.G. Morales-Guio, Electrochemical direct partial oxidation of methane to methanol, *Joule* 3 (2019) 2589–2593, <https://doi.org/10.1016/j.joule.2019.10.004>.
- [25] K. Shen, S. Kumari, Y.C. Huang, J. Jang, P. Sautet, C.G. Morales-Guio, Electrochemical oxidation of methane to methanol on electrodeposited transition metal oxides, *J. Am. Chem. Soc.* 145 (2023) 6927–6943, <https://doi.org/10.1021/jacs.3c00441>.
- [26] L. Arnarson, S. Schmidt, M. Pandey, A. Bagger, K.S. Thygesen, I.E.L. Stephens, J. Rossmeisl, Fundamental limitation of electrocatalytic methane conversion to methanol, *Phys. Chem. Chem. Phys.* 20 (2018) 11152, <https://doi.org/10.1039/c8cp01476k>.
- [27] S. Yamamoto, J.B. Alcauskas, T.E. Crozier, Solubility of methane in distilled water and seawater, *J. Chem. Eng. Data* 21 (1976) 78–80, <https://doi.org/10.1021/je60068a029>.
- [28] H. Tian, Y. Zhang, Z. Zhang, T. Lv, L. Bian, H. Wang, J. Li, Y. Yamauchi, Z.L. Wang, Selective radical oxidation of cyclohexane to adipic acid at electrochemical interfaces, *ChemCatChem* 15 (2022) e202201220, <https://doi.org/10.1002/cctc.202201220>.
- [29] Y. Feng, C. Jia, H. Zhao, K. Wang, X. Wang, Phase-dependent photocatalytic selective oxidation of cyclohexane over copper vanadates, *N. J. Chem.* 46 (2022) 4082–4089, <https://doi.org/10.1039/D1NJ05677H>.
- [30] Y. Zhang, Z. Yin, H. Hui, H. Wang, Y. Li, G. Liu, J. Kang, Z. Li, B.B. Mamba, J. Li, Constructing defect-rich V₂O₅ nanorods in catalytic membrane electrode for highly efficient oxidation of cyclohexane, *J. Catal.* 387 (2020) 154–162, <https://doi.org/10.1016/j.jcat.2020.04.023>.
- [31] J. Dai, W. Zhong, W. Yi, M. Liu, L. Mao, Q. Xu, D. Yin, Bifunctional H₂WO₄/TS-1 catalysts for direct conversion of cyclohexane to adipic acid: Active sites and reaction steps, *Appl. Catal. B: Environ.* 192 (2016) 325–341, <https://doi.org/10.1016/j.apcatb.2016.04.005>.
- [32] Y. Feng, C. Jia, H. Zhao, K. Wang, X. Wang, Phase-dependent photocatalytic selective oxidation of cyclohexane over copper vanadates, *N. J. Chem.* 46 (2022) 4082–4089, <https://doi.org/10.1039/D1NJ05677H>.

- [33] T. Kawada, T. Tajiri, H. Yamashita, M. Machida, Molten copper hexaoxodivanadate: an efficient catalyst for SO_3 decomposition in solar thermochemical water splitting cycles, *Catal. Sci. Technol.* 4 (2014) 780, <https://doi.org/10.1039/c3cy00880k>.
- [34] R. Jia, Y. Wang, C. Wang, Y. Ling, Y. Yu, B. Zhang, Boosting selective nitrate electroreduction to ammonium by constructing oxygen vacancies in TiO_2 , *ACS Catal.* 10 (2020) 3533–3540, <https://doi.org/10.1021/acscatal.9b05260>.
- [35] Y. Ding, L. Huang, J. Zhang, A. Guan, Q. Wang, L. Qian, L. Zhang, G. Zheng, Ru-doped, oxygen-vacancy-containing CeO_2 nanorods toward N_2 electroreduction, *J. Mater. Chem. A* 8 (2020) 7229–7234, <https://doi.org/10.1039/d0ta02211j>.
- [36] B. Liu, Z. Zheng, Y. Liu, M. Zhang, Y. Wang, Y. Wan, K. Yan, Efficient electrooxidation of biomass-derived aldehydes over ultrathin NiV-layered double hydroxides films, *J. Energy Chem.* 78 (2023) 412–421, <https://doi.org/10.1016/j.jechem.2022.11.041>.
- [37] K. Fan, H. Chen, Y. Ji, H. Huang, P.M. Claesson, Q. Daniel, B. Philippe, H. Rensmo, F. Li, Y. Luo, L. Sun, Nickel-vanadium monolayer double hydroxide for efficient electrochemical water oxidation, *Nat. Commun.* 7 (2016) 11981, <https://doi.org/10.1038/ncomms11981>.
- [38] Z. Li, J. Yang, Z. Chen, C. Zheng, L.Q. Wei, Y. Yan, H. Hu, M. Wu, Z. Hu, V “Bridged” Co-O to eliminate charge transfer barriers and drive lattice oxygen oxidation during water-splitting, *Adv. Funct. Mater.* 31 (2021) 2008822, <https://doi.org/10.1002/adfm.202008822>.
- [39] A. Prajapati, B.A. Collins, J.D. Goodpaster, M.R. Singh, Fundamental insight into electrochemical oxidation of methane towards methanol on transition metal oxides, *Proc. Natl. Acad. Sci. U. S. A.* 118 (2021) e2023233118, <https://doi.org/10.1073/pnas.2023233118>.
- [40] Y. Xu, D. Wu, P. Deng, J. Li, J. Luo, Q. Chen, W. Huang, C.M. Shim, C. Jia, Z. Liu, Y. Shen, X. Tian, Au decorated Pd nanowires for methane oxidation to liquid C1 products, *Appl. Catal. B* 308 (2022), <https://doi.org/10.1016/j.apcatb.2022.121223>.
- [41] M. Huang, S. Zhang, B. Wu, Y. Wei, X. Yu, Y. Gan, T. Lin, F. Yu, F. Sun, Z. Jiang, L. Zhong, Selective photocatalytic oxidation of methane to oxygenates over Cu-W- TiO_2 with significant carrier traps, *ACS Catal.* 12 (2022) 9515–9525, <https://doi.org/10.1021/acscatal.2c02424>.
- [42] E. Umeshbabu, G. Ranga Rao, A vanadium(V) oxide nanorod promoted platinum/reduced graphene oxide electrocatalyst for alcohol oxidation under acidic conditions, *Chemphyschem* 17 (2016) 3524–3534, <https://doi.org/10.1002/cphc.201600667>.
- [43] Q. Sun, J.M. Jehng, H. Hu, R.G. Herman, I.E. Wachs, K. Klier, In situ Raman spectroscopy during the partial oxidation of methane to formaldehyde over supported vanadium oxide catalysts, *J. Catal.* 165 (1997) 91–101, <https://doi.org/10.1006/jcat.1997.1446>.
- [44] H. Shen, Y. Zhao, L. Zhang, Y. He, S. Yang, T. Wang, Y. Cao, Y. Guo, Q. Zhang, H. Zhang, In-situ constructing of copper-doped bismuth catalyst for highly efficient CO_2 electrolysis to formate in ampere-level, *Adv. Energy Mater.* 13 (2022) 2202818, <https://doi.org/10.1002/aenm.202202818>.
- [45] Y. Chen, G. Zhang, H. Liu, J. Qu, Confining free radicals in close vicinity to contaminants enables ultrafast fenton-like processes in the interspacing of MoS_2 membranes, *Angew. Chem. Int. Ed.* 58 (2019) 8134–8138, <https://doi.org/10.1002/anie.201903531>.
- [46] S. Song, H. Song, L. Li, S. Wang, W. Chu, K. Peng, X. Meng, Q. Wang, B. Deng, Q. Liu, Z. Wang, Y. Weng, H. Hu, H. Lin, T. Kako, J. Ye, A selective Au-ZnO/ TiO_2 hybrid photocatalyst for oxidative coupling of methane to ethane with dioxygen, *Nat. Catal.* 4 (2021) 1032–1042, <https://doi.org/10.1038/s41929-021-00708-9>.
- [47] Y. Lyu, R. Xu, O. Williams, Z. Wang, C. Sievers, Reaction paths of methane activation and oxidation of surface intermediates over NiO on Ceria-Zirconia catalysts studied by In-situ FTIR spectroscopy, *J. Catal.* 404 (2021) 334–347, <https://doi.org/10.1016/j.jcat.2021.10.004>.
- [48] W. Sun, P. Wang, Y. Jiang, Z. Jiang, R. Long, Z. Chen, P. Song, T. Sheng, Z. Wu, Y. Xiong, V-Doped Cu_2Se hierarchical nanotubes enabling flow-Cell CO_2 electroreduction to ethanol with high efficiency and selectivity, *Adv. Mater.* 34 (2022) 2207691, <https://doi.org/10.1002/adma.202207691>.
- [49] S. Liu, X.F. Lu, J. Xiao, X. Wang, X.W. Lou, Bi_2O_3 Nanosheets grown on multi-channel carbon matrix to catalyze efficient CO_2 electroreduction to HCOOH , *Angew. Chem. Int. Ed.* 58 (2019) 13828–13833, <https://doi.org/10.1002/anie.201907674>.